Ionization Wave Propagation in a He Plasma Jet in a Controlled Gas Environment

Amanda M. Lietz[1], Edward V. Barnat[1], John E. Foster[2], and Mark J. Kushner[3]

[1] Sandia National Laboratories, Applied Optical and Plasma Sciences Department, 1515 Eubank Blvd. SE, Albuquerque, NM 87185, USA, amlietz@sandia.gov, evbarna@sandia.gov
[2] University of Michigan, Department of Nuclear Engineering and Radiological Sciences, 2355 Bonisteel Blvd., Ann Arbor, MI 48109-2104 USA, jefoster@umich.edu
[3] University of Michigan, Department of Electrical Engineering and Computer Science, 1301 Beal Ave., Ann Arbor, MI 48109-2122 USA, mjkush@umich.edu

Abstract

Characterizing ionization wave propagation in low temperature plasma jets is critical to predicting production of reactive species and plasma-surface interactions for biomedical applications and surface functionalization. In this paper, results from optical emission and laser induced fluorescence measurements of the ionization wave in a He plasma jet operating in a controlled gas environment are discussed, and used for comparison with numerical modeling. The ionization wave was observed using ICCD imaging, and characterized by time and spatially resolved electron density measurements using laser-collision-induced fluorescence (LCIF). The plasma jet was initially characterized using pure He (nominally at 200 Torr) while varying pressure and voltage. When operating in pure He, the ionization wave broadly expands exiting the plasma tube. Increasing the operating pressure reduces the speed and isotropic expansion of the ionization wave. The jet operated with a humid He shroud was also studied. The humid He shroud results in the electron density increasing and having an annular profile due to the lower ionization potential of H_2O compared to He and localized photoionization in the mixing region. Numerical modeling highlighted the importance of resonance radiation emitted by excited states of He, photoelectron emission from the quartz tube, and the kinetic behavior of the electrons produced by photoionization ahead of the ionization front.

I. Introduction

Atmospheric pressure plasma jets (APPJs) usually consist of a low temperature plasma sustained in a rare gas propagating into humid air. These devices are being widely researched for biomedical applications, such as cancer treatment and wound healing, and surface functionalization due to their low gas temperatures and customizable gas composition.[1–4] The plasma chemistry in these sources can be complex, including excited states and dissociation products of N_2, O_2, and H_2O, and the more stable species which occur by reactions of the dissociation products, including N_xO_y and HNO_x. The short lifetime and spatial nonuniformity of many of these species make measurements of their densities challenging. Advanced diagnostics have been used to measure species densities of H, O, OH, NO and O_3 in APPJs.[5–11] Even given these measurements of atomic and radical species to validate models, reaction pathways in these devices are in a large part derived from numerical modeling. Within these plasma chemistry models, the uncertainties in rate coefficients and cross sections used as input data can lead to significant uncertainties in the final predicted densities of reactive species.[12]

Validation of plasma models can be challenging due to the uncertainties in experimental measurements, the reaction mechanism and the input data used in the mechanism. The multiphysics nature of atmospheric pressure plasmas also increases the complexity of the models. Despite these challenges, a few studies have demonstrated agreement of models with density measurements of reactive species. Luo *et al*. used a 0-dimensional model to analyze the dominant pathways in a high electron density (~10^{16} cm^{-3}) plasma filament sustained in humid Ar.[13] The resulting OH and H densities were in agreement with time resolved measurements by laser induced fluorescence (LIF) and two-photon laser induced fluorescence (TALIF). Vasko *et al*. compared experimental measurements of H_2O_2 in an atmospheric pressure radiofrequency discharge with results from a 0-dimensional model and a 1-dimensional fluid model.[14] The 1-dimensional model provided more accurate H_2O_2 densities while both models indicated the same dominant pathways for production and loss of H_2O_2. Zhang *et al*. used a 0-dimensional model to calculate O_3 densities in an Ar plasma jet and compared these values to measurements by UV absorption.[10] The trends and magnitude of the O_3 density and the gas temperature were in agreement with experiment.

Several other studies have focused on validation of models (e.g. ionization wave propagation, electric fields). Tholin *et al*. validated a 2-dimensional fluid model by comparing optical

emission predicted by the model with ICCD imaging for a pin-to-pin discharge in atmospheric pressure air.[15] Viegas *et al*. conducted an experimental and modeling investigation of electric fields inside dielectric materials treated by an APPJ.[16] A target made of electro-optic material enabled measuring the spatially resolved electric field inside the target. The axial and radial electric fields calculated by the model agreed with the measured values. Dubinova *et al*. compared cylindrically symmetric fluid modeling with ICCD imaging of a streamer propagating toward and around a dielectric rod in air.[17] The model captured the inception cloud which forms before transition to streamer propagation.

Gas shrouds are annular gas flows having a different composition that surround a cylindrical plasma jet. The usual intent of gas shrouds is to isolate the plasm jet from ambient gases. Razavizadeh *et al*. found that the speed of ionization waves (IWs) increased when the gas surrounding a He plasma jet contained O_2 due to the photoionization of O_2 and electron detachment from anions.[18] Xian *et al.* observed that APPJs surrounded by molecular gas are more confined than those surrounded by a rare gas. More confinement of the plasma occurred with shrouds having attaching gases (air and O_2) than with N_2. Schmidt-Bleker *et al*. used experiments and modeling to compare the consequences of N_2 and air shield gases around a He APPJ.[19] The formation of anions reduced the radial spread of electrons into the shielding gas. Akman *et al*. reported that in an APPJ, a transition from a diffuse plasma in a pure He environment to a collimated jet occurred when the He plume was surrounded by air.[20]

In this paper, we compare time and spatially resolved measurements of the electron densities in a plasma jet incident onto an alumina target sustained in He to results from a 2-dimensional model. To enable use of laser-collision-induced fluorescence (LCIF) to measure electron densities, the system was primarily operated at reduced pressure (200 Torr) and in a simplified chemistry (pure helium and humid helium shrouds). The plasma jet consisted of two coaxial quartz tubes. The plasma is initiated inside the central tube where pure He flows. Gas can also be flowed through the outer tube to produce a shroud having different composition. Comparison of predictions from the model to experimental results emphasized the importance of resonant radiation from He to photoionization and photoelectron emission from the inner surface of the tube. The experimental results indicate that the molecular gases surrounding the rare gas plume enable ionization through Penning reactions and photoionization.

The experiment, including the design of the plasma jet and the LCIF analysis are de-

scribed in Sec. II. The geometry and initial conditions for the model are described in Sec. III. Sec. IV contains the experimental and modeling results, including a discussion of the consequences of pressure, applied voltage, humid shroud and flow rate. Concluding remarks are in Sec. V.

II. Description of the Experiment

A. Plasma Jet

The plasma jet used in this investigation, shown in Fig. 1, is a co-axial flow system designed to be vacuum compatible to enable operation in pure He environments. The electrode configuration was based on the work of Robert *et al*.[21] and is able to generate IWs which propagate in long tubes (10s of cm). The jet consists of two coaxial quartz tubes. He flows through the central tube as in a conventional plasma jet. The central tube has a 2 mm inner diameter (ID) and 4 mm outer diameter (OD). The outer tube has a 10.5 mm ID and a 12.7 mm OD, which produces an annulus of width 3.25 mm through which shroud gases flow. An annular powered electrode on the inside of the central quartz tube has an ID of 1.55 mm and an OD of 2 mm, to fit just within the center tube. The inner edge of the powered electrode where breakdown is expected to occur is rounded.

The grounded electrode was ultra-high-vacuum (UHV) compatible copper tape wrapped around the central tube. The tubes were mounted in a support structure made of polyether ether ketone (PEEK) which was 5.08 cm in diameter and 3.81 cm long. The two quartz tubes were mounted into a channel (shroud tube) and a hole (center tube) in the PEEK and sealed using vacuum epoxy. The PEEK support structure included connections for gas lines which provide separate gas flow through the central and shroud tubes.

A spacer between the inner and outer tubes at the end of the grounded electrode was PEEK with 8 equally spaced holes 1 mm in diameter which served to evenly distribute the shroud gases azimuthally while also keeping the two tubes properly centered and spaced. The applied voltage pulse was generated by a Directed Energy Inc. DEI PVX-4110 generator whose input voltage was provided by a Spellman SL600 power supply. The applied voltage pulse, shown in Fig. 2, has approximately a 100 ns rise time, a 140 ns fall, 430 ns duration and a +6 kV amplitude for the base case.

B. Vacuum System

The jet was operated in a cylindrical vacuum chamber with two 6" (15.24 cm) diameter flanges on the top and bottom, and eight 2¾" (6.98 cm) diameter flanges around the circumference. (The vacuum components from the manufacturer have English units. Their conversion to metric are in parenthesis.) The jet was mounted at the top of the chamber on a ½" (1.27 cm) diameter Ultra-Torr feedthrough attached to a 6" to 2¾" reducer flange. The system base pressure was approximately 20 mTorr, which indicates that at an operating pressure of 200 Torr, the minimum level of impurities was approximately 100 ppm.

While operating the jet, gases were pumped through a cylindrical manifold consisting of eight holes (1.25 mm in diameter) distributed around the jet at a radius of 3.84 cm. The manifold was connected to the vacuum system by a tube 1/4" (0.635 cm) in diameter. The conductance through this manifold was sufficient to operate as high as 1 standard liter per minute (slpm) while maintaining a gas flow which is essentially axially symmetric.

The target toward which the jet is directed is a 650 μm thick, 2.54 cm diameter disc of alumina backed with a metal film. This target was placed on a metal washer serving as ground which in turn was placed on a PEEK pedestal having a 3.1 cm diameter. The current through the ground electrode was measured using a Pearson Current Monitor (Model 2877).

C. Bubbler System

Two bubblers connected in series, shown in Fig. 1d, were used to humidify He feed gas to 100% relative humidity for use in the shroud. Both bubblers were made of borosilicate glass with a 40 mL capacity (Ace Glass Inc.) and sealed using Ace-Thread and Ultra-Torr fittings. The bubblers were operated with a gas dispersion tube having a fritted glass end with holes in the range 145-174 μm (Ace Glass Inc.). The first bubbler was heated with 7.2 W silicone heating tape. The second bubbler was kept at room temperature. Any water vapor above the vapor pressure condenses in this second bubbler, helping to ensure the gas leaving the second bubbler is near 100% relative humidity with a limited residence time in the bubbler system.

Three mass flow controllers (MFCs) were used, all supplied with pure He (99.999%). The first MFC supplied the central tube with He. The second MFC controlled the He which was mixed with the output of the bubbler system to tune the relative humidity of the shroud. The third MFC supplied the He which flowed through the bubbler. By adjusting the relative flow rates of the second and third MFCs, the humidity could be controlled while keeping the total

flow rate constant.

D. Laser-Collision-Induced Fluorescence

Laser-collision-induced fluorescence (LCIF) is a technique able to measure electron density and temperature in rare gas mixtures. LCIF has been developed for use in He at atmospheric pressure using the scheme shown in Fig. 3a.[22] In LCIF in He, a 389 nm laser excites the metastable He(2^3S) produced by the plasma to the He(3^3P) state. The He(3^3P) state will radiatively relax by emission of a 389 nm photon back to the He(2^3S) level, and this emission is referred to as laser induced fluorescence (LIF). In the presence of electrons, some of the He(3^3P) state can be collisionally excited to the He(3^3D) state by

$$e + He(3^3P) \rightarrow He(3^3D) + e. \quad (1)$$

This reaction has a threshold energy of only 0.06 eV and a rate coefficient which is relatively insensitive to the electron temperature. The He(3^3D) state then radiatively relaxes by emitting a 588 nm photon, which is referred to as laser-collision-induced fluorescence (LCIF). The ratio of the 588 nm LCIF to the 389 nm LIF can be used to determine the electron density. This technique is described in detail by Barnat, *et al*.[22]

A schematic of the setup used for LCIF measurements is shown in Fig. 1b. A mode-locked Ti:Sapphire laser produced 780 nm pulses with duration < 80 fs. At 1 kHz, one of these pulses is amplified by a Spectra-Physics Spitfire regenerative amplifier to approximately 2 mJ. The beam passes through a β-Barium borate (BBO) frequency doubling crystal reducing the wavelength to 390 nm. This BBO crystal was also used to fine-tune the wavelength to the transition at 388.9 nm. A 780 nm wave plate attenuated the 780 nm pump laser energy to produce a 388.9 nm laser energy of 15 - 20 μJ. Any remaining 780 nm light was removed from the beam using a pair of long wave pass mirrors that transmit 780 nm and reflect 388.9 nm. To produce a more uniform laser intensity and avoid illuminating the quartz tube, a set of lenses was used to increase the beam size which was then reduced by a series of apertures to ~7.5 mm. The circular beam passes through a cylindrical lens to generate a sheet of laser light which then passes through the plasma between the end of the central tube of the jet and the alumina surface. (The resulting intensity was less than 2 J/m^2 in the plasma.)

To reduce laser light scattering which can overwhelm the LIF signal, the sides of the central tube of the jet were blackened, and the inside of the vacuum chamber was covered in anodized aluminum foil. The windows through which the laser passed were at an angle adjusted to

reduce scattering signal and covered by antireflective coatings for 389 nm. Apertures inside the chamber were also used to block the scattered light. For each data set, the scattered laser light was measured by collecting images of the system with the plasma off, and this was subtracted from the LIF signal. When drift in the system caused the scattering to increase, the laser alignment was repeated.

The light from plasma emission, LIF, and LCIF was imaged using an Andor iStar camera using bandpass filters (10 nm FWHM) at 390 nm, 589 nm, 450 nm and 656 nm. The camera gate was 5 ns for all measurements.

E. Analysis of Laser-Collision-Induced Fluorescence Measurements

The LCIF data for the base case at 310 ns after start of the voltage pulse is shown in Fig. 3b. To obtain an electron density, it is necessary to take the ratio of the intensity of LIF signal emitted from He(3^3P) at 389 nm to the LCIF signal emitted from He(3^3D) at 588 nm. In the LIF and LCIF plotted in Fig. 3b, the emission from the plasma, the contribution of the laser scattering and the background have been subtracted. The ratio of these two signals is called the LCIF ratio, which is expected to be linearly proportional to the electron density for these conditions. Some portion of this LCIF ratio can be a result of collisions of the He(3^3P) state with the background gas,

$$\mathrm{He}(3^3\mathrm{P}) + \mathrm{He} \rightarrow \mathrm{He}(3^3\mathrm{D}) + \mathrm{He}. \qquad (2)$$

By collecting LCIF in the late afterglow when the electrons have thermalized (4.5 μs after the pulse) this contribution was experimentally determined. The contribution of this reaction to the LCIF ratio is proportional to the total background gas density, and has a value of (2×10^{-20} cm^3)n_{He}, where n_{He} is the density of He. This value has been subtracted from all LCIF ratios before converting the ratios to values of electron density.

The constant of proportionality required to convert the LCIF ratio to electron density must be derived as its value depends on the time delay from the laser pulse as well as the camera gate. Ohm's law was used to estimate the electron density. Since the current is constant, at any given height,

$$I = \frac{e^2}{m_e}\frac{N}{\upsilon_m}\frac{E}{N} n_e(z) A(z) \qquad (3)$$

where I is the current measured at the electrode under the alumina, e is the elementary charge, m_e

is the mass of electrons, N is the total number density of the background gas, υ_m is the momentum transfer collision frequency of electrons, and E is the electric field. $n_e(z)$ is the electron density and $A(z)$ is the cross-sectional area of the plasma at height z. This assumes that the majority of the current in the plasma is conduction current as opposed to displacement current.

E/N can be estimated from the ratio of the LCIF from the He(4^3D) state at 447 nm to that of the He(3^3D) state at 588 nm. The reaction e + He(3^3P) $\rightarrow$ e + He(4^3D), also shown in Fig. 3a, has a 0.74 eV threshold energy and a rate coefficient which is sensitive to electron temperature, T_e.[22] Assuming the local electric field approximation applies (T_e is at equilibrium with E/N) enables an estimate of E/N from this ratio. This ratio (emission from He(4^3D) over that of He(3^3P)), was previously measured in a configuration with a known E/N. Using the previous measurements as a calibration, E/N was estimated as approximately 2 Td (1 Td = 10^{-17} V-cm^2) at t = 310 ns. The rate coefficient for momentum transfer at 2 Td is approximately $\upsilon_m/N = 5 \times 10^{-8}$ cm^{3}s^{-1}.

In this plasma jet, the cross-sectional area of the plasma and the electron density (which is proportional to the LCIF Ratio) are functions of height. The diameter of the plasma at the center of the gap was estimated as the diameter containing 95% of the electrons based on the LCIF ratio. Based on these estimated values, an average electron density at the center of the gap was calculated.

An LCIF ratio of 1 is equivalent to an electron density of approximately 4×10^{12} cm^{-3}. Previously, the value of this conversion factor was estimated to be a factor of 3 higher (1.5×10^{13} cm^{-3}) for conditions where E/N was more controlled and better known. The conditions were a He pressure of 600 Torr, having a shorter camera gate and a shorter delay after the laser pulse.[23] The experimental electron densities discussed in this paper were derived using the calibration factor calculated here (4×10^{12} cm^{-3}).

The primary sources of error in this calibration factor are: the assumption in Eq. 3 that n_e is radially uniform, the estimation of E/N = 2 Td from 447 nm LCIF, and the value of υ_m/N. The nonuniformity could lead to an underestimate of this calibration factor by a factor of 2 or more. A 20% variation in E/N or υ_m/N would cause a commensurate error in the calibration factor. At low pressure, it is possible to estimate the conversion factor using a collisional radiative model [24]. However, in a more collisional plasma there is greater uncertainty in a larger number of processes. For these conditions, Ohm's law can be used to provide a reference point. Although

there is uncertainty in the value of the calibration factor, that uncertainty applies only to the absolute value of n_e. The relative values of n_e, and so their spatial dependencies, are not significantly influenced by this uncertainty.

The LCIF measurements rely on laser absorption by the He(2^3S) state. When the density of He(2^3S) is too low, a reliable electron density cannot be obtained from the LCIF data. He(2^3S) density is usually proportional to electron density in pure He, so it is expected that the electron density would be low in regions where the density of He(2^3S) is also low. From a procedure perspective, when the LIF intensity is not sufficiently above the background to produce a reliable density, the electron density was set to zero. We acknowledge that there is likely a low electron density in these regions which is simply not detectable by LCIF due to the low density of He(2^3S).

For each LCIF measurement, the number of pulses over which the data were collected was optimized for those particular conditions. The data were collected over a sufficient number of pulses to produce a reasonable signal to noise ratio in both the LIF and LCIF signals. Prior to the IW striking the target, LCIF data from approximately 10^6 pulses were averaged for each of the 588 nm and 389 nm wavelengths.

III. Description of the Model

The 2-dimensional hybrid plasma model used to model the plasma jet, *nonPDPSIM*, was described in detail by Norberg *et al*.[25] This model contains modules for solving Poisson's equation, fluid dynamics, radiation transport, and a Monte Carlo treatment of electrons emitted from surfaces. Poisson's equation was solved implicitly on an unstructured mesh, along with the transport of charged species and surface charging. The time step of this operation was automatically selected, typically 30 – 50 ps. The fluxes of charged species are calculated using the method of Scharfetter and Gummel [26], and the derivatives of these fluxes which make the implicit solution possible are described in Ref. [27]. The advective flow is addressed by solving the modified Navier-Stokes equations and charged and neutral species diffuse within this flow. The radiation transport calculation uses a Green's function operator, which accounts for an absorption mean free path which varies based on a nonuniform gas composition.

Boltzmann's equation is solved for electrons using a two-term spherical harmonic expansion of the electron energy distribution (EED) for the average composition in each zone of the

computational domain.[28] The zones of the computational domain are determined by a range of gas composition (for example, the mole fraction of H_2O). The resulting EED is used to generate a lookup table for a series of values for reduced electric field (*E/N*, electric field over number density) that relates the electron temperature (average electron energy) to reaction rate coefficients for electron impact reactions and transport coefficients. The electron energy equation is used to calculate the local electron temperature. The lookup table is then used to determine the value of the reaction rates and transport coefficients at each node on the mesh.

The electron Monte Carlo simulation (eMCS) was used to address electrons emitted from surfaces which are not accurately described by the fluid approximation. This can occur when the gradient in potential is large compared to the electron mean free path (at large *E/N* and low electron density). In the eMCS, a structured mesh is overlaid on the unstructured mesh on which the rest of the simulation is solved. The electric field is interpolated from the unstructured mesh onto the structured mesh. Electrons are emitted from surfaces as photoelectrons or ion-induced secondary electrons and given an initial energy of 4 eV. They are accelerated in the electric field and can undergo collisions based on the electron impact reactions included the reaction mechanism. As the electrons collide in the gas, if their energy decreases to below 3.6 eV, they are treated as a source of electrons in the bulk electron fluid. Any ions or neutral species produced by these eMCS electrons are treated as a source term in the respective fluid. The specific parameters for the eMCS model implemented for this paper are discussed in Sec. D.

A. Geometry and Initial Conditions

The cylindrically symmetric geometry used in the model is shown in Fig. 4. The dimensions match that of the experiment as closely as possible. The central quartz tube has ID = 2 mm and OD = 4 mm. The shroud tube has ID = 10.5 mm and OD = 12.7 mm. Both quartz tubes have a dielectric constant of $\varepsilon_r = 4$. All metals are perfect conductors, and all dielectrics are perfect insulators. The ground electrode around the central tube in the computational geometry is thicker than the copper tape used in the experiment to avoid an excessively fine mesh. The target is 650 μm thick alumina ($\varepsilon_r = 10$) which rests upon a 500 μm thick ground electrode. This ground electrode is also thicker than that of the experiment to avoid a prohibitively fine mesh. The target rests on a PEEK pedestal ($\varepsilon_r = 4$) which is 4 cm in diameter.

The geometry of the vacuum chamber which surrounds the gas was also included in the computational mesh. The grounded surface surrounding the jet in the experiment was composed

of the Ultra-Torr feedthrough, the reducer flange, and the chamber (refer to Fig. 1b). These features have been included in the computational geometry as a single ground electrode. The pump is an annulus at the bottom of the chamber, which is consistent with the pumping manifold in the experiment. This surface uses a constant pressure boundary condition which is 200 Torr for the base case.

The computational geometry does differ from the experimental setup in the following way. The length of the powered and ground electrode around the inner tube were increased by 3 cm (i.e. the electrodes extend further into the tube). While using the same electrode configuration, this elongation decreases computational time by reducing the distance the IW needs to propagate through the tube from 8.5 to 5.5 cm. Computational tests have shown that the qualitative behavior of the IW is generally the same in this geometry as in the case when the IW must propagate the full distance (the electron density is within 20%).

The numerical mesh is shown in Fig. 5, and includes 36,427 nodes, 20,907 of which are in the plasma. The mesh size is approximately 52 μm above the alumina surface and 65 μm in the tube. Several refinement zones expand the mesh size to as large as 1.2 mm far from where the plasma occurs.

In the base case, 500 sccm of He/H_2O = 99.95/0.05 flows through the central nozzle with there being no flow through the shroud nozzle. The steady state flow dynamics are established by calculating the fluid dynamics and neutral transport only for at least 30 ms before initializing the plasma pulse. The applied voltage is a +6 kV pulse with a 100 ns rise time which is consistent with the pulse applied in the experiment.

B. Reaction Mechanism

The electronic excited states of helium that are explicitly included in this reaction mechanism are $He(2^3S)$, $He(2^1S)$, $He(2^3P)$ and $He(2^1P)$. The higher states are grouped into He(3P) and He(3S). All of the He excimers are grouped into a single species, He_2*. The resulting reaction mechanism contains the species listed in Table 1. The reaction mechanism for H_2O is that of Van Gaens *et al*.,[29] with the He reactions with water derived species from Norberg *et al*.[30] A humid gas mixture was used in all cases even when no intentional water admixture was included to represent outgassing and impurities in the vacuum system that result in some residual H_2O vapor. In humid plasmas, even with unintentional water impurities, water cluster ions can make up a significant portion of the ions in the plasma.[31] To limit the computational burden,

only a limited water cluster ion chemistry was included, with a maximum of one added water molecule for each ion. In practice, more complex clusters may form in these conditions.

C. Photoionization Model

With the applied voltage having positive polarity, the IW is highly sensitive to photoionization for propagation. In helium discharges, photons having high enough energy to ionize water include emission from electronically excited states (He*) relaxing to the ground state, and radiation from the excimers (He_2*). The emission from these states can ionize all impurities, and the dominant impurity was assumed to be H_2O, having a photoionization cross section of approximately 2.3×10^{-17} cm^2 at a wavelength of 58.4 nm.

In these simulations, the radiation transport was included for two or three photons. Emission at 58.4 nm and 53.7 nm from He(2^1P) and the lumped state He(3P) was included in all simulations, and emission at 81 nm from He_2* was included in limited simulations for testing. The photons emitted from He(2^1P) and He(3P) [which includes He(3^1P)] have the highest intensity. These two photons can be reabsorbed by ground state He atoms, and therefore are trapped in the plasma with a short absorption mean free path of approximately 10 nm. Pressure broadening results in photons in the wings of the lineshape function escaping the plasma.[32] The radiation trapping factor is the average number of times a photon is emitted and reabsorbed before escaping the plasma volume. Using the method of Holstein [33] and the analytical solutions by van Trigt [34] for an infinite cylindrical plasma, the trapping factor is estimated to be 900 for the 58.4 nm transition from the He(2^1P) state. The Einstein emission coefficient for He(2^1P) in the reaction mechanism was divided by this trapping factor, and only the photons emitted in the wings of the lineshape function that escape from the plasmas are tracked using the radiation transport module. He(3P) is also a significant source of photoionization. Since this is a lumped state, it was assumed that the most abundant excited state is that having the lowest energy, He(3^1P). The radiation trapping factor and Einstein emission coefficient are based on He(3^1P). The result is that 53.7 nm radiation from the He(3^1P) state has a trapping factor of 620, which was used to modify the effective emission coefficient of He(3P) in the reaction mechanism.

Due to the computational expense of the radiation transport calculations, only emission from the He(2^1P) and He(3P) states were included in the results presented here. Photoionization resulting from emission from He_2* was also included for a limited number of cases and was found to be insignificant (smaller than that of He(2^1P) by a factor of 10^3) and therefore was not

included. However, at higher pressure, photoionization from He_2* may become more significant as the rate of conversion of He* to He_2* increases with pressure (He* + He + M $\rightarrow$ He_2* + M).

The concentration of impurities in the system determines the rate of photoionization ahead of the IW and therefore has important consequences on the IW dynamics. The concentration of impurities is expected to be at least 0.01% (100 ppm) for the base pressure, though is likely larger during operation because outgassing H_2O has a longer residence time at the operating pressure than when the vacuum system is pumped down to the base pressure. The concentration of H_2O impurity in the model was selected to provide sufficient preionization ahead of the IW to sustain the IW. An impurity concentration of 0.05% H_2O was used for the pure He flowing through the central tube, a value that provided qualitative agreement with speed and shape of IWs measured in the experiment. At this concentration of impurity, the mean free path for photoionization is approximately 13 cm, meaning that most photons exit the plasma region without ionizing gas.

Photoelectron emission from the surfaces of the quartz and the alumina was also included in the model. The materials were assumed to be completely opaque to the VUV photons in the radiation transport model. Experimental measurements of the photoelectron yield for quartz are approximately 3% for photons greater than 10 eV.[35] However, better qualitative agreement with the IW shape in the tube were achieved with a photoelectron yield of 2%, which was the value used in this work.

D. Electron Monte Carlo Model

For the base case, only the electrons emitted from the alumina surface were addressed using the eMCS. Electrons emitted from the quartz surface were treated using fluid equations, except as noted below, in which the secondary electrons from a surface node are apportioned among the nearest neighbor mesh points in the plasma. The structured mesh on which the eMCS is executed extends from the surface of the alumina to 6.9 mm above that surface and extends to a radius of 8.5 mm. The eMCS calculation begins before the IW enters this region, at t = 300 ns after the start of the voltage pulse, and the eMCS is performed every 1 ns. 150 electron pseudoparticles are emitted from each surface mesh point during each update to the eMCS with an initial energy of 4 eV. These parameters are sufficient for the results to be independent of the extent of the eMCS mesh, the update frequency, and the number of pseudoparticles. Electrons produced by electron impact ionization by secondary electrons in the eMCS were also treated as

particles in the eMCS. This approach is important since as the IW approaches the alumina surface, *E/N* in the region between the alumina and the IW is high (~10^{-16} V-cm^2 or 10 Td).

In select cases where the photoelectron yield of the quartz tube was varied, the eMCS was also used inside the tube for photoelectrons and secondary electrons emitted from the quartz. In this case the eMCS mesh extends from the powered electrode to the end of the quartz tube and extending to a radius of 1 mm. The eMCS calculation begins at t = 0.5 ns and is updated every 1 ns.

IV. Properties of Ionization Waves: Experiment and Model

A. Experimental Base Case

Optical emission from the plasma in the base case is shown in Fig. 6. Note that the plasma emission is obtained from all light which reaches the ICCD, and has not been Abel inverted to account for the cylindrically symmetric plasma. The IW emerges from the tube at 190 ns, implying an average IW speed inside the tube of 4×10^7 cm/s assuming the initial formation time is negligible. (All times are relative to the start of the voltage pulse.) The plasma outside the tube expands nearly isotopically from 190 ns to 205 ns. During this time, the IW speed slows to approximately 2×10^7 cm/s. As the front of the IW approaches the alumina surface, the field enhancement is stronger in regions near the axis, causing the portion of the IW closer to the axis to propagate faster (3×10^7 cm/s) with more intense emission. Meanwhile, the speed of the portion of the IW that is at further from the axis (r > 1.4 mm) decreases, creating the shape at 210-225 ns.

As the IW reaches the surface, the intensity of emission in the plasma column from the lower half of the gap increases. This occurs when a conductive channel forms between the powered electrode and the dielectric, which in this case has a relatively large capacitance (280 pF). The mechanism of this increased light emission which propagates in the reverse direction is analogous to a restrike and has been observed in other plasma jets.[36]

After the IW contacts the surface, a surface ionization wave (SIW) forms and propagates radially outward along the surface. This SIW produces emission in a layer approximately 350 μm thick and spreads along the surface at an average speed of 6×10^6 cm/s. The restrike also propagates back toward the powered electrode, causing the densities of electrons and electronically excited states inside the tube to increase, resulting in a brighter plasma in the tube seen at 250 ns.

As the IW contacts the alumina at 220 ns, the current measured at the grounded electrode under the alumina increases, as shown in Fig. 2. Before this time, there is still a nonzero current due to the displacement current as the IW approaches the surface and the electric field increases. As the SIW spreads, the surface of the alumina charges. As the applied voltage begins to fall at 360 ns, the current at the ground electrode under the alumina target becomes negative. The positive charge that has accumulated on the alumina surface is neutralized by current in the plasma flowing in the opposite direction during this period. The magnitude of this current is smaller than that of the forward current, but the duration is longer (several microseconds).

The electron densities measured using LCIF in the base case are shown in Fig. 7. In aligning the laser, it was necessary to maintain some gap between the bottom of the quartz tube and the top of the laser sheet to prevent scattering of laser light off the tube which would overwhelm the LIF measurement. Therefore the region approximately 500 μm beneath the tube was outside the measurement region. Pixels with an LIF signal that is not significantly above the background noise are excluded. The maximum electron density at 200 ns is 4×10^{11} cm^{-3} during the isotropic expansion period. Just before the IW contacts the surface (210 ns), the electron density in the center of the plasma has increased to 7×10^{11} cm^{-3}. (This value was obtained from smoothing the data.) The shape of the electron density profile reflects that of the plasma emission at this time. After the IW contacts the surface the electron density in the bulk plasma increases by 40% to 1×10^{12} cm^{-3} in 15 ns.

At 250 ns, after the SIW has spread to a radius of 3.1 mm, there is a region of elevated electron density near the alumina surface. The electron density near the surface is approximately 3×10^{12} cm^{-3} compared to 6×10^{11} cm^{-3} in the bulk plasma. The electron density in the bulk plasma continues to increase as the SIW spreads across the surface, with the electron density reaching 1×10^{12} cm^{-3} by 310 ns.

There is an experimental artifact in the n_e measurements at 210 and 225 ns in Fig. 7. When the laser is applied to the plasma to make the LCIF measurements, there may be a small perturbation in the IW speed. The effect is small enough that it is generally not apparent in time resolved ICCD imaging of plasma emission (i.e., it does not affect the qualitative behavior of the IW). However, this momentary increase in IW speed can cause an overestimate in the electron density at the front of the IW. When the LCIF measurements are taken, an equivalent plasma emission image (without the laser) is used to subtract the light emitted by the plasma. If the IW

in this plasma emission image is slightly slower than that of the LIF and LCIF data, there will be an artificial increase in the measured LIF and LCIF at the front of the IW. The interpretation that the elevated LCIF ratios at the front of the IW are not due to electrons is consistent with the expected discharge dynamics, because the recombination rate is slow enough in pure He (even with a small amount of impurities) that the electron density would not be expected to decrease significantly in 15 ns.

B. Model Base Case

The computed behavior of the IW as it propagates out of the tube and toward the alumina surface is shown in Fig. 8. As the IW propagates in the tube, the electric field over the gas number density (E/N) is as high as 7×10^{-15} V-cm^2 (700 Td). This elevated E/N results in an electron temperature (T_e) as high as 18 eV in the front of the IW, and an electron impact ionization rate (S_e) of 6×10^{21} cm^{-3}s^{-1}. The IW speed in the model is approximately a factor of 3 slower than in the experiment. As a result, the IW does not emerge from the tube until 335 ns. The duration of the voltage pulse in the model is extended to keep the voltage at its maximum value while the IW contacts the alumina. That is the voltage fall is not included in the model.

As the IW passes a given point in the tube, the electron density (n_e) increases to approximately 1×10^{13} cm^{-3}. Just after the IW exits the tube, the plasma remains confined to $r < 2$ mm. As the IW approaches the surface, E/N, T_e, and S_e increase as the voltage drop occurs over a smaller gap and the electric field increases. After contact with the surface, a restrike occurs resulting in an increase in the electron density in the gap to 2×10^{13} cm^{-3} by $t = 425$ ns (30 ns after the IW has contacted the surface). Although the magnitude of n_e is higher than the measured value, the factor of 2 increase with the restrike is similar to the 40% increase seen in the experiment. An SIW with a thickness of approximately 290 μm (compared to 350 μm in the experiment) spreads radially outward along the surface with $S_e \approx 1 \times 10^{20}$ cm^{-3}s^{-1}. The electron density in the SIW reaches 9×10^{12} cm^{-3} at $t = 425$ ns, approximately a factor of 3 larger than in the experiment. Though the isotropic expansion observed in the optical emission in Fig. 6 is not as apparent in the model, the same qualitative behavior occurs. The shape of the plasma at $t = 215$ ns (Fig. 6) in the experiment resembles S_e at $t = 393$ ns in the model.

The modeling investigation has brought to our attention the importance of several physical mechanisms in the dynamics of this plasma jet. The ionization processes which occur ahead

of the IW as it propagates across the gap are shown in Fig. 9. The ionization rates in this figure are taken from along the axis at 389 ns, when the IW is 2.8 mm above the alumina surface. The electrons in this simulation are divided into two groups. Most of the electrons in the model are treated as a fluid and are referred to as bulk electrons. The electrons emitted from the alumina surface, and their progeny (generated by electron impact ionization) are addressed kinetically using the eMCS. When the energy of the electrons in the eMCS decreases below 3.6 eV, they are converted into bulk electrons. The majority of the electrons in the plasma are generated by electron impact ionization of the bulk fluid electrons. However, the ionization which occurs ahead of the IW is critical in sustaining and controlling its propagation. Photoionization of impurity H_2O occurs ahead of the IW at a rate of ~3×10^{15} $cm^{-3}s^{-1}$. Electrons which are emitted from the alumina surface produce electron impact ionization ($S_e(Secondary) \approx 9 \times 10^{15}$ $cm^{-3}s^{-1}$) as they are accelerated toward the IW by the electric field. This rate is on the order of the electron impact ionization rate by electrons in the bulk fluid ($S_e(Bulk) \approx 3 \times 10^{16}$ $cm^{-3}s^{-1}$). Within 1 mm of the IW, $S_e(Bulk)$ and $S_e(Secondary)$ are several orders of magnitude larger due to a higher electric field. Though the electron density ahead of the IW is low, $n_e \approx 3 \times 10^7$ cm^{-3}, these electrons provide an initial source which undergoes exponential growth in the high electric field of the IW.

To demonstrate the importance of using a kinetic treatment for the electrons emitted from the alumina, the modeling results for n_e and S_e are compared with and without the eMCS in Fig. 10. When the eMCS is not used, electrons emitted from the surface are immediately included in the bulk fluid electrons. Before 355 ns, the S_e and n_e are similar for both simulations, but as the IW approaches the alumina surface, the behavior diverges. When the eMCS is not used, S_e in the IW is lower, and the IW speed decreases as it approaches the surface. This behavior is unexpected, as the higher electric field should lead to an acceleration of the IW. The electron density in the SIW is also an order of magnitude higher when the eMCS is used. Using the eMCS makes it more consistent with the qualitative behavior of n_e in the experiment, in which n_e in the SIW is a factor of 5 larger than that of the bulk. This comparison suggests that treating electrons produced ahead of the IW as part of the bulk fluid for these conditions (200 Torr of He) is not always adequate to accurately capture the IW dynamics. It may be more accurate to expand the eMCS methods to address the transport of electrons produced by photoionization ahead of the IW as well.

The average IW speed inside the tube in the model is 1.4×10^7 cm/s (compared to 4×10^7 cm/s in the experiment). This speed is still lower than that observed in the experiment in spite of the powered electrode being closer to the target, which increases the average IW speed. This slower IW in the model may be due to the simplified electron dynamics in the model, where only the secondary electrons are treated kinetically, but not the electrons produced ahead of the IW by photoionization. The effect of treating electrons kinetically has previously been demonstrated for streamer propagation.[37]

The IW propagates from the tube to the target in 54 ns (1.5×10^7 cm/s) compared to 30 ns in the experiment. The SIW speed agrees in the model and the experiment for the first 30 ns of contact (6×10^6 cm/s), but the SIW slows during the restrike in the model. This discrepancy may be a result of some residual charge on the surface in the experiment from previous voltage pulses.

The isotropic expansion of the IW that is observed in the experiment as the IW exits the tube is not as apparent in the current modeling results. There are two probable reasons for this discrepancy. In the model, a single pulse is simulated, but in the experiment, the jet is repetitively pulsed at 1 kHz. Though the gas flow flushes out much of the remaining species in the tube, the residence time is longer further from the axis where the gas flow is lower. It is possible that more water cluster ions or excited states survive locally at larger radii, and promote radial propagation. The second possibility is that limiting the eMCS to electrons that originate from surfaces is not accounting for the fact that the electrons produced ahead of the IW by photoionization are likely to be more isotropic, and may be accelerated rapidly enough to require them to be treated kinetically.

Photoelectron emission from the surface of the quartz tube was critical for sustaining an IW in the tube. The IW was simulated with several different values of the photoelectron yield for the quartz tube, and the results are shown in Fig. 11. The density of He(3P), a lumped state which can emit visible light, is plotted to approximate the plasma emission. For these cases, the photoelectrons and secondary electrons from the inner surface of the quartz tube were treated with the eMCS. The photoelectron yield in the model determined whether the plasma in the tube formed on the axis or propagated as a surface ionization wave along the quartz surface, making it annular in shape. A higher photoelectron yield produced an annular IW. The electrons that are produced ahead of the IW are critical for directing the propagation of the IW. The source of

these electrons is primarily photoionization or photoelectron emission from surfaces. When the photoelectron yield is 0%, the electron density ahead of the IW is larger on axis. When the photoelectron yield is large (> 2%), the electron density ahead of the IW is larger closer to the inner surface of the quartz tube. The density of He(3P) most consistent with the observations in the experiments occurs with a photoelectron yield of 1%. The photoelectron yield does affect the IW speed inside the tube, with the speed increasing by 40% as the photoelectron yield increases from 0% to 5%.

C. Pressure

The experimental emission from the IW for different pressures is compared in Fig. 12. The IW speed is sensitive to pressure, so rather than a constant pulse duration, the voltage pulse was held at the maximum voltage for 80 ns after the IW first contacted the surface for consistency with the base case. This results in pulse durations of 370, 430, 640, 840, 1090, and 1340 ns for 150, 200, 300, 400, 500, and 600 Torr. The electron density was measured 30 ns after the plasma first contacted the alumina surface for each pressure, and the results are shown in Fig. 13.

At low pressure the IW emission intensity is low before contact with the surface. Generally, higher pressures reduce the role of diffusion in the discharge and allow for steeper gradients. As the pressure increases, the electron mobility decreases. The potential gradient at the leading edge of the IW and the maximum electric field increases. After the IW passes, T_e decreases more rapidly as electrons lose energy through collisions. Therefore as the pressure increases, the plasma emission is more localized at the front of the IW and the tail of emission behind the IW front is shorter, as shown in Fig. 12.

The restrike is more apparent and induces a greater increase in plasma emission at lower pressures (a factor of 7 at 150 Torr compared to a factor of 2 at 600 Torr). At low pressure, the plasma is more conductive and the current increases more rapidly. The current measured at the target 30 ns after the IW contacts the surface is 28 mA for 150 Torr compared to 3.4 mA for 500 Torr. Because the restrike is weaker and less total charge is transferred to the target as pressure increases, the SIW covers a smaller area.

The IW also becomes more confined to the axis as the pressure increases. At higher pressure, the relative concentration of impurities may be similar, leading to a higher absolute density of impurities. The radiation trapping factors are, to first order, independent of pressure when collisional broadening dominates, which is the case in He at these pressures. The effect of

the line broadening (which decreases trapping) is balanced by the increase in absorber densities (which increases trapping), resulting in the trapping factor being independent of pressure. At higher pressure, the density of H_2O is larger and the characteristic absorption length is shorter. Therefore at higher pressure, photoionization occurs closer to the IW than it would at lower pressure. The result is a more focused IW which does not expand as rapidly when it exits the tube.

The surface ionization wave becomes confined to a thinner layer above the alumina as the pressure increases. This layer is 600 μm thick at 150 Torr, and 180 μm thick at 600 Torr. As the pressure increases, the mobility of charged species decreases, and steeper gradients can be maintained near the alumina surface. This confinement of the SIW to a thinner layer is also apparent in the electron density measurements shown in Fig. 13.

As the pressure increases, the evolution of the electron density 30 ns after the IW contacts the surface is non-monotonic. The electron densities in the center of the gap are 1.2×10^{12}, 7.5×10^{11}, 1.1×10^{12}, 1.4×10^{12}, 2.2×10^{12}, and 6.4×10^{11} cm^{-3} for 150, 200, 300, 400, 500, and 600 Torr, with the maximum occurring at 500 Torr. The electron density in the SIW follows a similar pattern of decreasing then increasing as the pressure increases. This trend is a result of changes in both the cross-sectional area of the plasma and the total current (and, similarly, the total energy deposition). As the pressure increases, the conductivity decreases, and the power deposition decreases, which is expected to decrease the inventory of electrons produced. However, as the pressure increases, the plasma is also confined more to the axis, and the energy deposition occurs in a smaller volume (increasing the energy density), which is expected to increase the electron density. These competing processes result in the non-monotonic behavior.

D. Voltage

The effect of applied voltage on the IW was also experimentally investigated using ICCD imaging and LCIF measurements. The optical emission from the experiment for voltages of 4 kV and 6.5 kV is shown in Fig. 14. The pulse duration was again adjusted so that the voltage remains at its maximum for 80 ns after the IW contacts the surface; the voltage rise time was unchanged. The IW speed increased with the applied voltage (from 1.9×10^7 to 5.0×10^7 cm/s in the tube) due to a higher *E/N*. The IW speed in the tube was estimated based on the time at which the IW is first visible outside the tube from the ICCD imaging.

At each voltage investigated, there is a transition from isotropic expansion to a surface-directed IW, but the vertical position of this transition change depends on the applied voltage.

This transition occurs 4.3 mm above the alumina surface for 4 kV and 2.7 mm for 6.5 kV (based on optical emission). With a higher applied voltage, the electron temperature is higher; there is more isotropic IW propagation and a later transition to a surface-directed IW.

Increasing the applied voltage increases T_e, resulting in an increase in the plasma emission from the IW. There is also an increase in the intensity of the restrike which occurs when the plasma contacts the alumina surface. At higher voltage, the electron density in the tube is expected to be higher before the IW reaches the alumina, resulting in a larger conductivity. Therefore when the IW contacts the surface, the current increases more rapidly, and more energy is deposited in the plasma.

The electron density measured by LCIF 30 ns after the IW contacts the surface for each voltage is shown in Fig. 15. The electron density measured at 6 kV in Fig. 15 is higher than that shown in Fig. 7 by approximately a factor of 2. For all of the LCIF measurements in Fig. 15, the bubbler system was connected to the chamber. While vacuum chamber was separated from the bubbler system by valves, some of the additional vacuum components increased the leak rate and therefore the impurity levels in the gas.

The electron density in the central plasma column outside of the quartz tube is not particularly sensitive to the applied voltage. The diameter of this column of elevated electron density increases with the applied voltage, because the SIW spreads to larger radius (3.7 mm compared to 1.6 mm) in the 30 ns of contact for higher applied voltage. This allows the plasma to conduct a larger current for higher applied voltage. At lower voltage, n_e on the axis is elevated near the target, while at higher voltage it is relatively uniform along the axis. At higher voltage, a faster SIW has resulted in a larger plasma diameter in the 30 ns of contact with the surface generating a wider column of plasma.

E. Humid Shroud

For applications, most APPJs are used to treat surfaces in an ambient air environment. The presence of surrounding molecular gases has been shown to significantly influence the IW propagation dynamics.[18,20] To investigate the influence of the ambient in a more controlled system with a simplified chemistry, a shroud flow of 500 sccm was introduced, with varying He/H_2O mixtures using the bubbler system.

The plasma emission for 2.3% H_2O in the shroud at 389 nm from $He(3^3P)$ and at 656 nm from H_α emission is shown in Fig. 16. The IW speed as it crosses the gap is 4×10^7 cm/s com-

pared to 2.5×10^7 cm/s for the base case. With a humid shroud, photoionization produces electrons ahead of the IW primarily at the interface between the He and the humid He shroud. Once the IW reaches this mixing region, direct electron impact ionization of H_2O can be more rapid than that of He because it has a lower ionization potential (12.6 eV compared to 24.6 eV) provided that the concentration of H_2O is low enough that T_e remains high. Penning ionization of H_2O by He* also contributes to an increased ionization rate in this mixing region. These effects all contribute to the IW propagating at a higher speed. The plasma emission from He(3^3P) appears to be annular in shape, with a SIW which is faster than in the base case, taking 20 ns to reach a radius of 3 mm rather than 30 ns in the base case.

In the presence of molecular gases, several assumptions used in analysis of the LCIF measurements for pure He should be revisited. First, in using LCIF to measure the electron density, it is assumed that only electrons and ground state neutrals produce excitation from He(3^3P) to He(3^3D). The rate of excitation by H_2O is assumed to be the same as that of He and is subtracted from the LCIF ratios. The contribution to the LCIF ration from any other species with densities several orders of magnitude lower than that of He (H, OH, H_2O(v), etc.) is expected to be much less than that of the He.

Another effect of added water vapor at sufficient concentrations is a reduction in the density of the metastable He(2^3S). The generation rate of He(2^3S) can be reduced by the decrease in electron temperature that occurs with sufficient H_2O concentration. He(2^3S) is also rapidly quenched by Penning ionization,

$$He(2^3S) + H_2O \rightarrow He + H_2O^+ + e, \qquad (4)$$

with a reaction rate coefficient of 1.1×10^{-10} cm^3s^{-1}. This quenching limits the lifetime of He(2^3S) to 61 ns at 2.3% H_2O at 200 Torr. Therefore in regions of higher H_2O concentration, the electron density is not observable by LCIF due to there being insufficient He(2^3S) densities. In Fig. 17, the LIF and LCIF emissions are shown, along with the LCIF ratio for a jet with a humid shroud. The LCIF ratio is not calculated for pixels in which the LIF signal is not significantly above the background. In these regions, the electron density may still be elevated, but it is not detectable because of the insufficient He(2^3S) density.

A third effect of water vapor is the sensitivity to the H_2O density of the electron impact reaction rate which is critical for LCIF. In order for LCIF measurements to be accurate the rate coefficient for electron impact excitation from He(3^3P) to He(3^3D) (Eq. 1) should be independent

of both *E/N* and the H_2O mole fraction. The EED was calculated for different concentrations of water vapor using a two-term spherical harmonic expansion and the same cross section set which was used for the 2-dimensional simulations. Then the cross section for the reaction in Eq. 1 from Shevelko *et al*. was used to calculate the reaction rate at different values of *E/N*, shown in Fig. 18.[38] Since the reaction in Eq. 1 has a low threshold energy of 0.06 eV (electrons at 300 K are 0.026 eV), the reaction rate coefficient becomes independent of *E/N* above approximately 1.8 Td in pure He. With 1% H_2O in He, the rate is independent of *E/N* above approximately 4 Td (T_e = 2.1 eV). Between 1.8 Td and 4 Td there are some differences in the rate coefficient, leading to an underestimate of the electron density by as much as a factor of 2 when the humidity is 2.3%. The electron temperature is expected to be greater than 0.45 eV (*E/N* = 2 Td) for the conditions discussed here. The end result is that LCIF can be used to measure the electron density, though the electron density may be underestimated in humid regions.

The electron density measurements by LCIF for varying levels of shroud humidity are shown in Fig. 19. "Pure He" refers to when the valves to the bubbler system are closed, and "0% H_2O" is the condition where the valves to the bubbler system are open, but no gas flows through the bubbler. Though the lowest humidity in the shroud investigated was nominally pure He, the leak rate of the bubbler system was significantly higher than that of the chamber and the impurity concentration is expected to be higher than in the base case. As a result, the IW emerged from the tube 15 ns earlier than in the base case, and the electron density was approximately 80% higher.

Increasing the mole fraction of H_2O in the shroud from pure He to 0.1% results in an increase in n_e from 1×10^{12} to 2×10^{12} cm^{-3}, but the maximum electron density remains on axis. In this range, an increase in humidity decreases the radius of the plasma, because the electron density is higher, and the cross-sectional area required to conduct the same amount of current is smaller. As the mole fraction of water in the shroud increases from 0.1% to 0.25%, the maximum electron density no longer occurs on the axis. The electron density is a maximum in a conical region which represents the mixing zone between the He flowed through the central tube and the humid He in the shroud. As the humidity of the shroud continues to increase, n_e on the axis decreases. At 0.75% H_2O, n_e in the mixing zone is a factor of 2.5 larger than n_e on the axis in the center of the gap. Photoionization and Penning ionization rates are higher in this mixing layer, resulting in preferential propagation of the IW in this region.

As the humidity exceeds 0.75%, the electron density in the SIW decreases near the axis. For 1.5% H_2O in the shroud, n_e in the SIW is approximately 3×10^{12} cm^{-3} for $r < 1$ mm compared to 9×10^{12} cm^{-3} for $r > 1$ mm. This indicates that the IW is annular as it contacts the alumina surface and primarily spreads outward away from the axis. This behavior is not apparent in the optical emission in Fig. 16 because this emission is not Abel inverted. The portion of the SIW propagating toward the camera makes the SIW appear as a disc rather than a ring.

F. Humid Shroud Modeling

Electron density and ionization source from the model for an IW with a humid shroud are shown in Figs. 20 and 21. With a humid shroud, the IW becomes annular after exiting the tube, and propagates more quickly, which is consistent with the experimental observations. S_e and n_e for the base case and with 1.5% H_2O in the shroud are compared in Fig. 20 when the IW is at the same position (which is not necessarily at the same time).

With 1.5% H_2O in the shroud, the IW reaches the end of the tube 30 ns earlier than in the base case, which is consistent with the experiment. The IW speed inside the tube is the same in both cases until it approaches within 2.5 mm of the end of the tube. After this point with the humid shroud, the IW speed increases from 1.4×10^7 to 1.9×10^7 cm/s and begins to move off the axis. This acceleration is a result of greater production of electrons ahead of the IW which produce ionization as they are accelerated toward the IW.

The level of H_2O impurities inside the tube is the same for both cases (diffusion of H_2O into the tube is negligible). When the IW is still 2.5 mm from the end of the tube ($t = 293$ ns), the photoionization rate in the gap 6 mm ahead of the IW is more than a factor of 2 larger with a humid shroud. At this time, n_e in the gap is a factor of 3 larger with a humid shroud (4.2×10^6 compared to 1.4×10^7 cm^{-3}) and is annular compared to radially uniform for the base case. The photoionization rate is largest in the regions where the gradient from pure He to humid He is the steepest, immediately outside the tube outlet at $r = 1$ mm. The photoionization rate in this region reaches 2×10^{16} $cm^{-3}s^{-1}$ as the IW approaches the outlet of the tube.

The IW propagates across the gap faster with the humid shroud, taking 30 ns (2.6×10^7 cm/s) compared to 54 ns (1.5×10^7 cm/s) in the base case. This increase in speed by a factor of 2 is consistent with the experimental observations, though the model underestimates the IW speed in both cases.

With 1.5% H_2O in the shroud, the IW is already annular as it emerges from the tube. This shape is consistent with the experimental observations in Fig. 16, where the plasma emission appears annular immediately upon exiting the tube. The IW maintains this annular shape as it propagates across the gap, though the radius decreases as the IW approaches the surface. The electric field on axis increases as the IW approaches the surface, increasing the electron impact ionization rate at smaller radii.

The gradients at the front of the IW are less steep with the humid shroud. Therefore *E/N* is lower, and the maximum value of S_e is lower. There are two factors which contribute to a lower *E/N* in the IW. First, the preionization is greater with a humid shroud. This means the conductivity of the air ahead of the IW is greater, and unable to sustain high fields. Second, the geometry of the IW determines the electric field enhancement. When the IW is on axis, as in the base case, the electric field enhancement is much greater than when the plasma is annular (and the effective radius is larger). As a result, the model indicates that n_e is lower in the presence of a humid shroud. This trend is inconsistent with the experimental results in which n_e increases by a factor of 3 in the presence of a humid shroud. For 1.5% H_2O in the shroud, n_e at the midpoint of the gap is 1×10^{12} cm^{-3} in the model compared to 4×10^{12} cm^{-3} in the experiment. This discrepancy may be due to photodetachment from negative ions remaining from previous pulses, which are not included in the simulations which address only a single pulse.

The computed electron density 30 ns after the IW contacts the surface is shown in Fig. 21 for comparison with the experimental results in Fig. 19. The electron density with the shroud at 0.05% H_2O (the same gas composition as the base case), remains maximum on the axis, consistent with the experimental results. The electron density profile is similar to that of 0% H_2O in Fig. 19. The plasma rapidly transitions to a more annular shape as the humidity of the shroud is increased in the model. Some initial indication of an annular shape appears at 0.1%, and the n_e profile is clearly annular when the humidity is increased to 0.25% H_2O. This behavior is generally in agreement with the LCIF measurements, though in the experiment there is no indication of the transition to an annular shape at 0.1%.

G. He Flow Rate

With 2.3% H_2O at 500 sccm in the shroud, the flow rate of the pure helium in the central tube was varied from 300 to 700 sccm to highlight the role of H_2O as it diffuses into the pure He. At a low flow rate, the H_2O diffuses to the axis, as shown by the modeling results of the steady

state profiles in Fig. 22. Increasing the flow rate of the central He results in flushing out the H_2O and decreasing its mole fraction on the axis. The residence time of the He inside the tube is 13 ms for 300 sccm and 5 ms for 700 sccm.

LCIF measurements of electron density for different central He flow rates are shown in Fig. 23. The electron density in all cases is highest in the mixing region between the He and the humid He. The electron density is also generally larger for low flow rates, where Penning ionization and electron impact ionization of H_2O can occur more rapidly due to the higher mole fraction of H_2O that has diffused into the He. As the flow rate increases to 700 sccm, the electron density profile becomes nearly annular, rather than conical when the H_2O has sufficient time to diffuse into the He flow.

V. Concluding Remarks

A helium plasma jet in a controlled atmosphere in contact with an alumina target was investigated using ICCD imaging, laser-collision-induced fluorescence measurements of electron density, and numerical modeling. In the experiments performed in pure He, the IW spreads as it exits the end of the tube, expanding almost isotropically. Upon approaching the alumina surface, the portion of the IW closest to the axis accelerates and intensifies due to enhancement of the electric field. Upon contacting the alumina target, a surface ionization wave develops and the dielectric surface charges as the plasma expands radially.

In this positive polarity plasma jet, the propagation of the IW is sensitive to photoionization of impurities and photoelectron emission from the dielectric tube which produce electrons ahead of the IW. Photoionization by the resonant photons emitted from He(2^1P) and He(3^1P) are more important than those emitted by the excimer. A higher photoelectron yield from the inside surface of the tube resulted in a more annular plasma inside the tube. Photoelectron emission from the alumina target helped sustain the IW as it approached the target surface. At 200 Torr in pure He, kinetic effects of the electrons become significant ahead of the IW where the electric field is large, and the fluid approximation may not accurately represent the IW behavior. This is especially critical as the IW approaches the target surface and E/N is large.

Increasing the pressure of the plasma jet results in an IW which is more confined to the axis of the jet. As the pressure increases, the diffusivity and mobility of electrons decreases, and larger gradients develop. The front of the IW and the surface ionization wave are confined to thinner layers. The restrike that occurs when the IW contacts the target is less intense because

the conductivity of the plasma is lower.

Humidity in a shroud surrounding the He jet results in a transition of the IW outside from being on the axis to annular. The speed of the IW also increases with humidity in the shroud because of the contributions of Penning ionization and the lower ionization energy of H_2O compared to He. The preionization due to photoionization which occurs ahead of the IW has an annular profile with a maximum in the mixing region between the pure He and the humid. Changing the flow rate of the pure He in the central tube can tailor the position of the maximum electron density by changing the profile of the gas composition outside of the tube. The IW preferentially propagates at the interface between the He and the surrounding molecular gas. Overall, the combination of experimental and modeling results has provided insights into the physical processes that are important in plasma jet devices.

Data Availability

The data that support the findings of this study are available from the corresponding author upon reasonable request.

Acknowledgements

This material was based upon work supported by the U.S. Department of Energy, Office of Science, Office of Fusion Energy Sciences under award numbers DE-SC000319 and DE-SC0020232, the US Department of Energy Office of Science Graduate Student Research Program, the National Science Foundation (PHY-1902878) and the NSF Graduate Research Fellowship Program. Sandia National Laboratories is a multimission laboratory managed and operated by National Technology & Engineering Solutions of Sandia, LLC, a wholly owned subsidiary of Honeywell International Inc., for the U.S. Department of Energy's National Nuclear Security Administration under contract DE-NA0003525. This paper describes objective technical results and analysis. Any subjective views or opinions that might be expressed in the paper do not necessarily represent the views of the U.S. Department of Energy or the United States Government.

References

[1] H.-R. Metelmann et al., Clin. Plasma Med. **9,** 6 (2018).
[2] P. Dimitrakellis and E. Gogolides, Adv. Colloid Interface Sci. **254,** 1 (2018).
[3] K. Y. Cheng, Z. H. Lin, Y. P. Cheng, H. Y. Chiu, N. L. Yeh, T. K. Wu and J. S. Wu, Sci. Rep. **8,** 1 (2018).
[4] A. J. Knoll, P. Luan, A. Pranda, R. L. Bruce and G. S. Oehrlein, Plasma Process. Polym. **15,** 1 (2018).
[5] S. Yatom, Y. Luo, Q. Xiong and P. J. Bruggeman, J. Phys. D. Appl. Phys. **50,** 415204 (2017).
[6] N. Knake, S. Reuter, K. Niemi, V. Schulz-von der Gathen and J. Winter, J. Phys. D. Appl. Phys. **41,** 194006 (2008).
[7] T. Verreycken, R. Mensink, R. van der Horst, N. Sadeghi and P. J. Bruggeman, Plasma Sources Sci. Technol. **22,** 055014 (2013).
[8] S. Yonemori, Y. Nakagawa, R. Ono and T. Oda, J. Phys. D. Appl. Phys. **45,** 225202 (2012).
[9] Y. Sakiyama, N. Knake, D. Schröder, J. Winter, V. Schulz-von der Gathen and D. B. Graves, Appl. Phys. Lett. **97,** 151501 (2010).
[10] S. Zhang, W. van Gaens, B. van Gessel, S. Hofmann, E. Van Veldhuizen, A. Bogaerts and P. Bruggeman, J. Phys. D. Appl. Phys. **46,** 205202 (2013).
[11] A. F. H. van Gessel, K. M. J. Alards and P. J. Bruggeman, J. Phys. D. Appl. Phys. **46,** 265202 (2013).
[12] M. M. Turner, Plasma Sources Sci. Technol. **24,** 035027 (2015).
[13] Y. Luo, A. M. Lietz, S. Yatom, M. J. Kushner and P. J. Bruggeman, J. Phys. D. Appl. Phys. **52,** 044003 (2019).
[14] C. A. Vasko, D. X. Liu, E. M. van Veldhuizen, F. Iza and P. J. Bruggeman, Plasma Chem. Plasma Process. **34,** 1081 (2014).
[15] F. Tholin, D. L. Rusterholtz, D. A. Lacoste, D. Z. Pai, S. Celestin, J. Jarrige, G. D. Stancu, A. Bourdon and C. O. Laux, IEEE Trans. Plasma Sci. **39,** 2254 (2011).
[16] P. Viegas, E. Slikboer, A. Obrusník, Z. Bonaventura, A. Sobota, E. Garcia-Caurel, O. Guaitella and A. Bourdon, Plasma Sources Sci. Technol. **27,** 094002 (2018).
[17] A. Dubinova, D. Trienekens, U. Ebert, S. Nijdam and T. Christen, Plasma Sources Sci. Technol. **25,** 055021 (2016).
[18] S. Razavizadeh, H. Ghomi and A. Sobota, Plasma Sources Sci. Technol. **27,** 075016 (2018).
[19] A. Schmidt-Bleker, S. A. Norberg, J. Winter, E. Johnsen, S. Reuter, K. D. Weltmann and M. J. Kushner, Plasma Sources Sci. Technol. **24,** 035022 (2015).
[20] M. A. Akman and M. Laroussi, IEEE Trans. Plasma Sci. **41,** 839 (2013).
[21] E. Robert, V. Sarron, D. Riès, S. Dozias, M. Vandamme and J.-M. Pouvesle, Plasma Sources Sci. Technol. **21,** 034017 (2012).
[22] E. Barnat and A. Fierro, J. Phys. D. Appl. Phys. **50,** 14LT01 (2017).
[23] E. V Barnat and A. S. Fierro, in preparation (2019).
[24] E. V. Barnat and K. Frederickson, Plasma Sources Sci. Technol. **19,** 055015 (2010).
[25] S. A. Norberg, E. Johnsen and M. J. Kushner, Plasma Sources Sci. Technol. **24,** 035026 (2015).
[26] D.L. Scharfetter and H. K. Gummel, IEEE Trans. Electron Devices **16,** 64 (1969).
[27] A. M. Lietz and M. J. Kushner, Plasma Sources Sci. Technol. **27,** 105020 (2018).

[28] A. M. Lietz, X. Damany, E. Robert, J.-M. Pouvesle and M. J. Kushner, Plasma Sources Sci. Technol. **28,** 125009 (2019).
[29] W. Van Gaens and A. Bogaerts, J. Phys. D. Appl. Phys. **47,** 079502 (2014).
[30] S. Norberg, PhD Thesis, Modeling atmospheric pressure plasma jets: plasma dynamics, interaction with dielectric surfaces, liquid layers and cells, (University of Michigan, 2015).
[31] S. Große-Kreul, S. Hübner, S. Schneider, A. von Keudell and J. Benedikt, EPJ Tech. Instrum. **3,** 6 (2016).
[32] N. A. Roberds, M. M. Hopkins, B. T. Yee, A. Fierro and C. H. Moore, Phys. Plasmas **27,** 043507 (2020).
[33] T. Holstein, Phys. Rev. **72,** 1212 (1947).
[34] C. van Trigt, Phys. Rev. A - At. Mol. Opt. Phys. **13,** 726 (1976).
[35] T. H. Distefano and D. E. Eastman, Solid State Commun. **9,** 2259 (1971).
[36] T. Darny, J. M. Pouvesle, V. Puech, C. Douat, S. Dozias and E. Robert, Plasma Sources Sci. Technol. **26,** 045008 (2017).
[37] J.-M. Guo and C.-H. Wu, J. Phys. D. Appl. Phys. **26,** 487 (1993).
[38] V. P. Shevelko and H. Tawara, *Cross Sections for Electron-Impact Induced Transitions Between Excited States in He; n, n'=2, 3, and 4*, (National Institute for Fusion Science, 1995).

Figure Captions

1. Schematic of the experimental setup. (a) Plasma jet design. (b) Vacuum chamber and LCIF beams. (c) Photo of the plasma jet in contact with an alumina surface. (d) Schematic of the water bubbler system.
2. The applied voltage pulse and the current measured at the electrode under the alumina target for the base case. The delay from the start of the voltage pulse to the current rise at the target is due to the time required for the ionization wave to propagate through the jet and to the target.
3. LCIF Properties. (a) He triplet states which are relevant to the analysis of the LCIF diagnostic. (b) Laser-induced fluorescence (LIF), laser-collision-induced fluorescence (LCIF), and their ratio plotted from 0 to 1.25 on a linear scale for the base case at t = 310 ns.
4. The geometry used in the modeling investigation. a) Entire computational domain. b) Enlargement of electrode and shroud. The central tube has a 2 mm inner diameter and a 4 mm outer diameter. The distance from the end of the tube to the alumina surface is 7.85 mm.
5. The computational mesh used to model the plasma jet. a) Entire computational domain. b) Enlargement near the substrate. The mesh size is approximately 52 μm at the alumina surface and 65 μm in the tube.
6. ICCD imaging of ionization wave propagation in the base case. Time is measured from the start of the voltage pulse and the camera gate was 5 ns. Filters were applied to image emission at 389 nm (from He(3^3P)) and 589 nm (from He(3^3D)).
7. Electron densities measured by LCIF. Time is measured from the beginning of the voltage pulse. The maximum value in each frame is noted.
8. Modeling results of the ionization wave as it propagates across the gap between the end of the tube and the surface, and forms a surface ionization wave along the alumina. *E/N* is the electric field over the number density on a 2-decade log scale, T_e is the electron temperature on a linear scale, S_e is the electron impact ionization from the bulk electrons on a 4-decade log scale, and n_e is the electron density on a 3-decade log scale.
9. The sources of electrons and electron density between the ionization wave and the alumina surface. This data is extracted along the z-axis at t = 389 ns. At this time, the front of the IW is on the is 2.8 mm above the alumina surface. The IW position and direction are indicated by the dashed box. $S_{Penning}$ is the Penning ionization rate, S_{photo} is photoionization, $S_{e(Bulk)}$ is

electron impact ionization by the fluid electrons, S_e*(Secondary)* is the electron impact ionization by the secondary electrons predicted by the eMCS. S_{sec} is the electrons emitted from the surface (secondary electrons and photoelectrons).

10. Plasma properties with kinetic secondary electrons. (left) The electron impact ionization rate (S_e) and (right) the electron density (n_e) of the IW when applying the electron Monte Carlo simulation to electrons emitted from the alumina surface (eMCS) and by treating the electrons emitted from the surface as part of the bulk electron fluid (no eMCS). Densities are plotted on a 3-decade log scale.
11. Density of the lumped state He(3P) inside the tube from the model with different photoelectron yields of the quartz tube. The density of He(3P) is expected to be proportional to total light emission. Results are at 149 ns after the start of the voltage pulse when the IW is approximately halfway between the electrodes and the outlet of the tube. The IW travels faster for larger photoelectron yields, and so the results are plotted for different axial positions for each frame (2.9 cm above the alumina for 0% and 3.5 cm above the alumina for 5%).
12. ICCD imaging of all emission (unfiltered) from the plasma jet operated at (left) 400 Torr and (right) 600 Torr. The pulse duration was increased with pressure.
13. The electron density measured by LCIF 30 ns after the IW has contacted the surface at different pressures. For each frame, the maximum value of the electron density is indicated above each frame.
14. ICCD imaging of all light (unfiltered) for (left) 4 kV and (right) 6.5 kV. The camera gate was 5 ns and the images are averaged over 5,000 pulses for 4 kV and 400 pulses for 6 kV.
15. The electron density measured by LCIF 30 ns after the IW contacts the alumina surface for different voltages.
16. ICCD imaging of optical emission from a plasma jet with a 2.3% H_2O in the shroud. Filters are used to image emission from (left) He(3^3P) and (right) H_α. The gate is 5 ns and the images are averaged over 14,000 pulses for 389 nm and 15,000 pulses for 656 nm.
17. Laser-induced emission for a plasma jet with 2.3% H_2O in the shroud. (top) The laser induced fluorescence (LIF) signal and (center) the laser-collision-induced fluorescence (LCIF) signal in arbitrary units on a linear scale. (bottom) The ratio of the LCIF to the LIF signal is only calculated for pixels where the LIF intensity exceeds that of the background noise. The LCIF ratio is plotted on a linear scale from 0 to 2, which is equivalent to an electron density

from 0 to 8×10^{12} cm^{-3}.

18. Reaction rate coefficient of e + He(3^3P) $\rightarrow$ He(3^3D) + e as a function of *E/N* for He with different levels of H_2O impurities. Using LCIF emission as a measurement of electron density requires that this rate is relatively insensitive to *E/N*. Based on this result, the impact of H_2O on the validity of LCIF should be minimal with less than 2.3% H_2O.
19. Electron density measured by LCIF for pure He in the central tube and varying humidity in the shroud tube. "Pure He" refers to when the valves to the bubbler system are closed, and "0% H_2O" is the condition where the valves to the bubbler system are open, but no gas flows through the bubbler. The total flow in the shroud tube is held constant at 500 sccm. The densities are plotted on a linear scale. With >1% H_2O, regions of high H_2O density have insufficient He(2^3S) densities to measure electrons by LCIF.
20. Modeling results of (left) electron impact ionization rate, S_e, and (right) electron density, n_e, for the base case ("Base") and with a shroud having 1.5% H_2O in He ("H_2O shroud"). The IW travels faster with the humid shroud, however the results are plotted when the IW is at the same position. The time in nanoseconds is indicated on the frame for each plot of S_e. The results of n_e are plotted for the same times.
21. Electron density (n_e) calculated by the model for varying shroud humidity plotted on a 2-decade log scale. The mole fraction of H_2O in the shroud is indicated above each frame. The IW propagates faster for a higher humidity in the shroud, and the results are compared 30 ns after the IW contacts the surface. This occurs at 425, 409, 391, 381, 375, 371, 367, and 349 ns for 0.05%, 0.1%, 0.25%, 0.5%, 0.75%, 1%, 1.5%, and 2.3%
22. The H_2O composition calculated by the model for 500 sccm of He/H_2O = 97.7/2.3 in the shroud and pure He in the main tube. The central flow is 300 sccm (left) and 700 sccm (right).
23. Electron densities measured by LCIF for a jet with 500 sccm of He/H_2O = 97.7/2.3 in the shroud and varying flow rate of pure He in the central tube. Densities are plotted on a linear scale.

Table 1. Species Included in the Model.

Ground State Neutrals	He, H_2O, H, H_2, O, O_2, OH, H_2O_2, HO_2
Positive Ions	He^+, He_2^+, H^+, H_2^+, H_3^+, O^+, O_2^+, O_4^+, H_2O^+, H_3O^+, OH^+, $H_2O^+(H_2O)$, $H_3O^+(H_2O)$, $O_2^+(H_2O)$
Negative Ions	e, H^-, O_2^-, O^-, OH^-, $O_2^-(H_2O)$, $O^-(H_2O)$, $OH^-(H_2O)$
Excited States	He(2^3S), He(2^1S), He(2^3P), He(2^1P), He(3P), He(3S), He_2*, H*, H_2(r), H_2(v), H_2*, O_2(v), O_2(r), $O_2(^1\Delta)$, , $O_2(^1\Sigma)$, O(^{1}D), H_2O(v), OH*

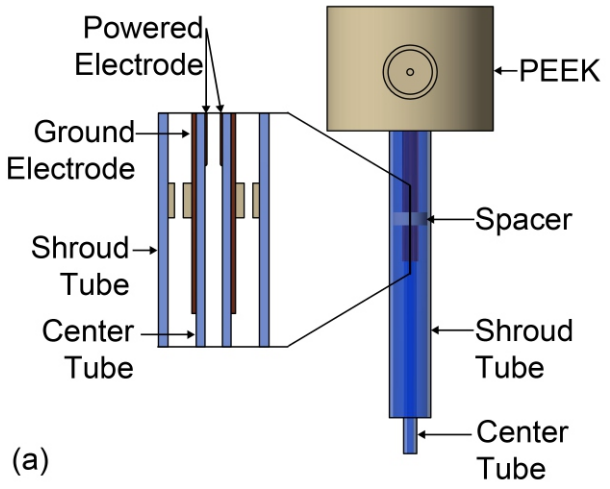

(a)

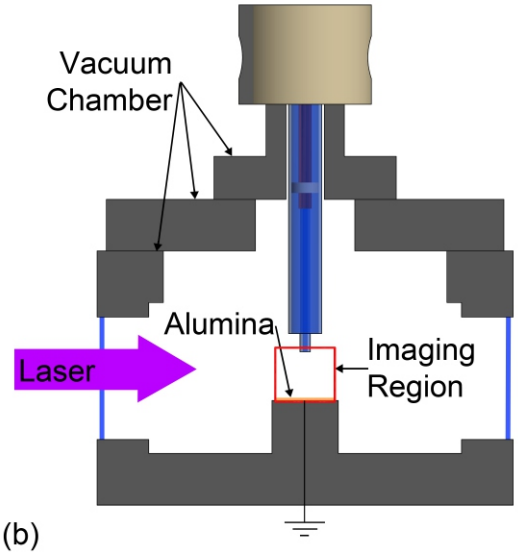

(b)

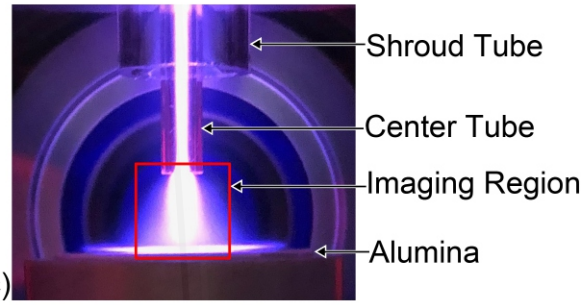

(c)

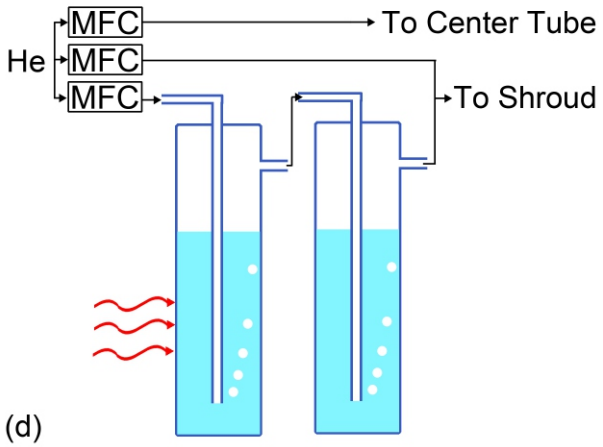

(d)

Lietz et al
Jet controlled
Fig 1 of 23

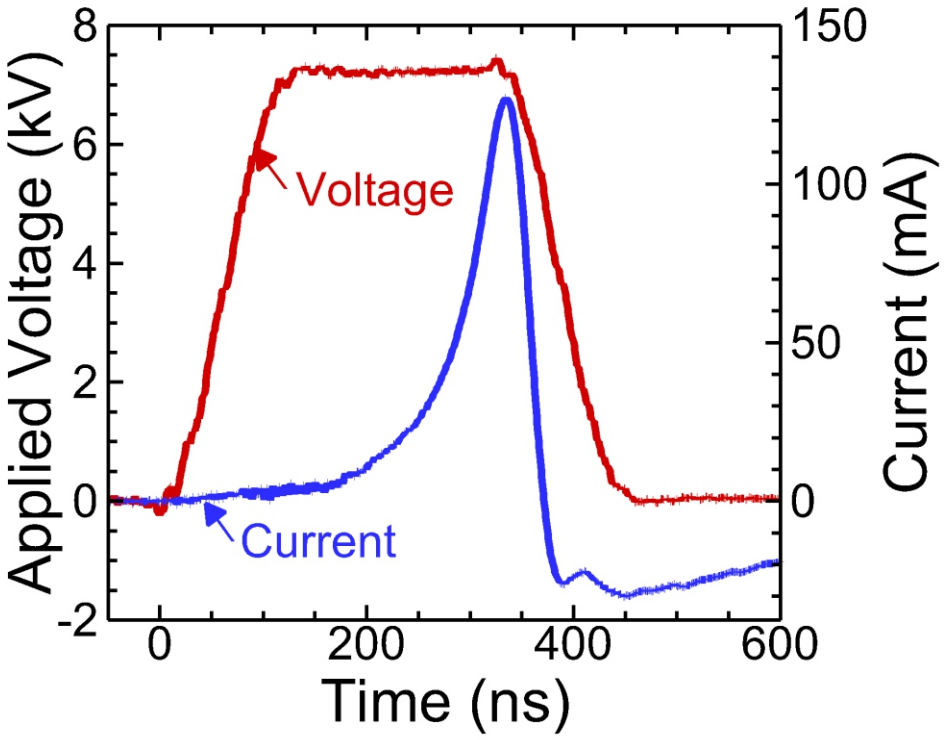

Lietz et al
Jet controlled
Fig 2 of 23

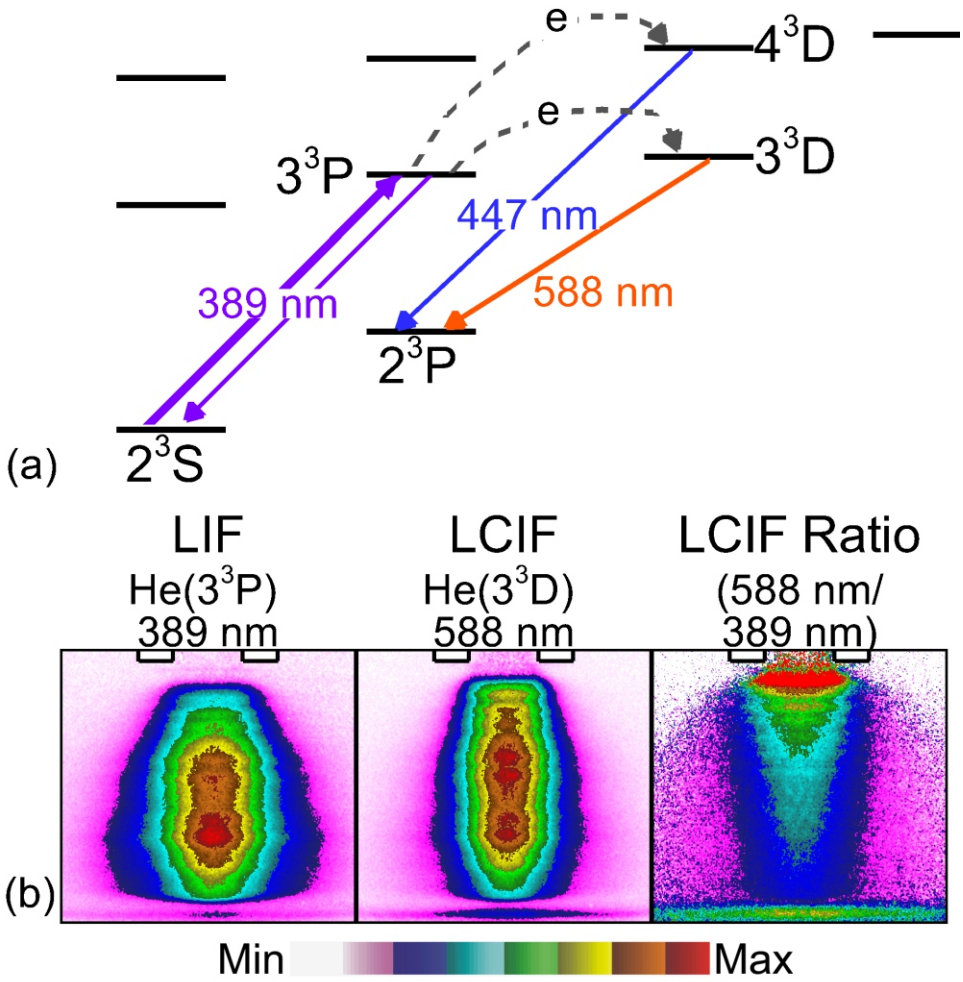

Lietz et al
Jet controlled
Fig 3 of 23

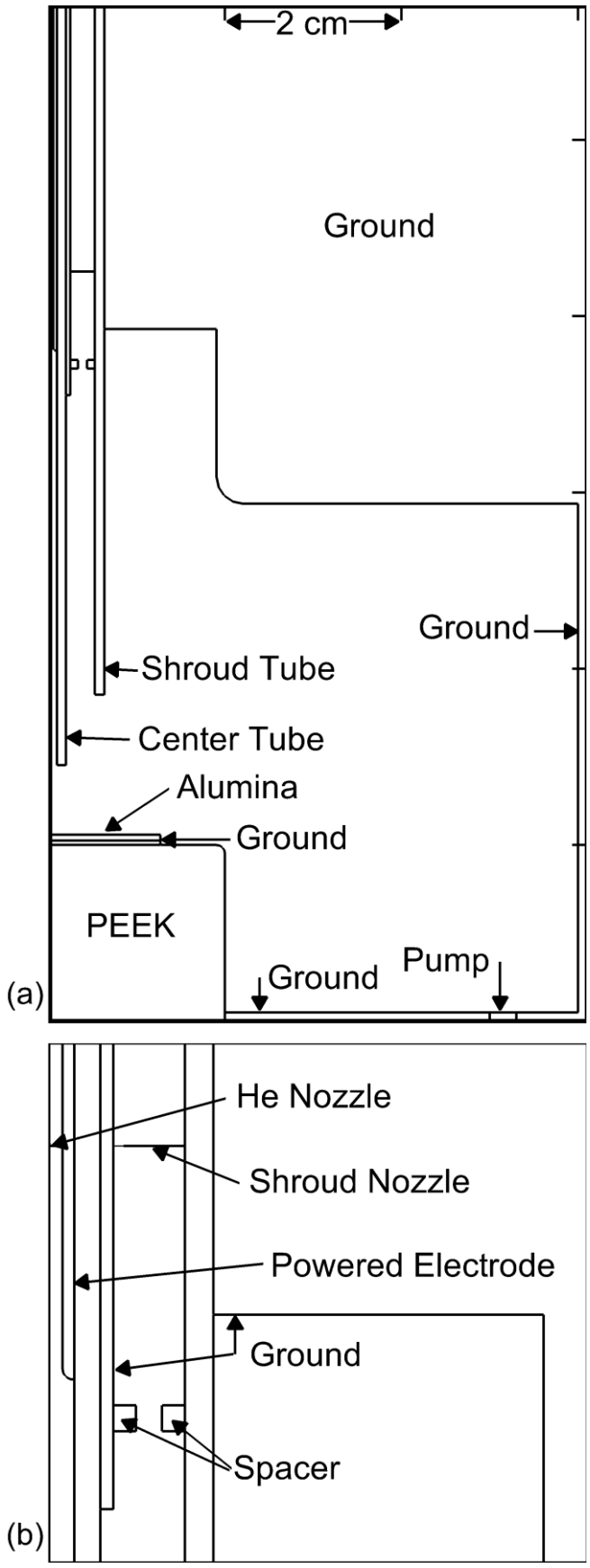

Lietz et al
Jet controlled
Fig 4 of 23

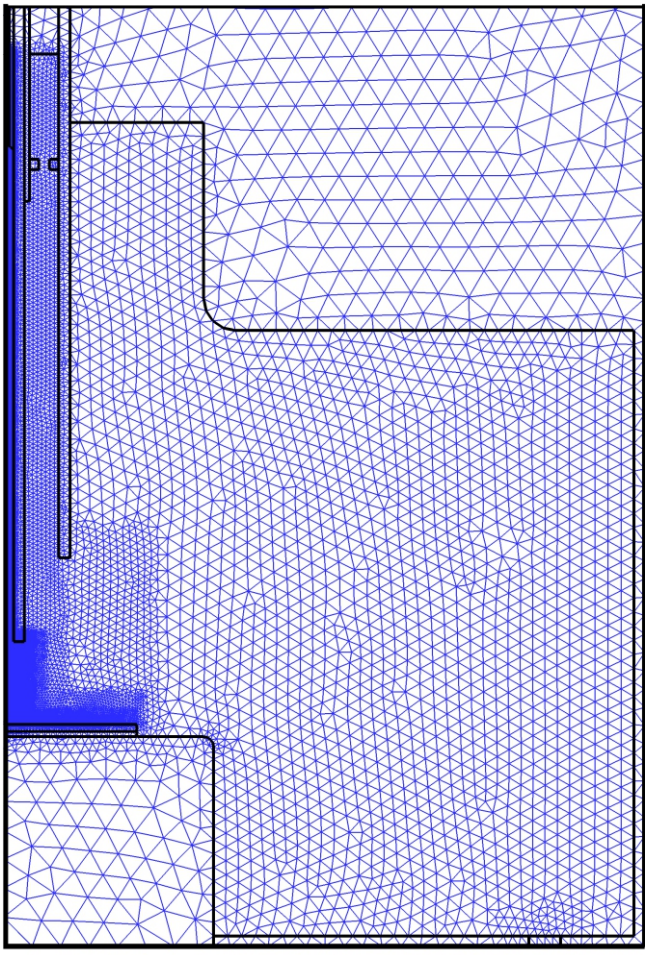
(a)

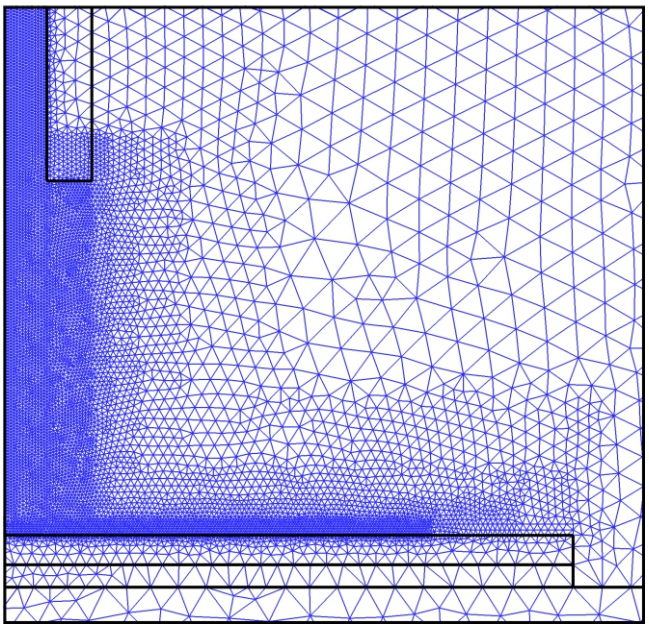
(b)

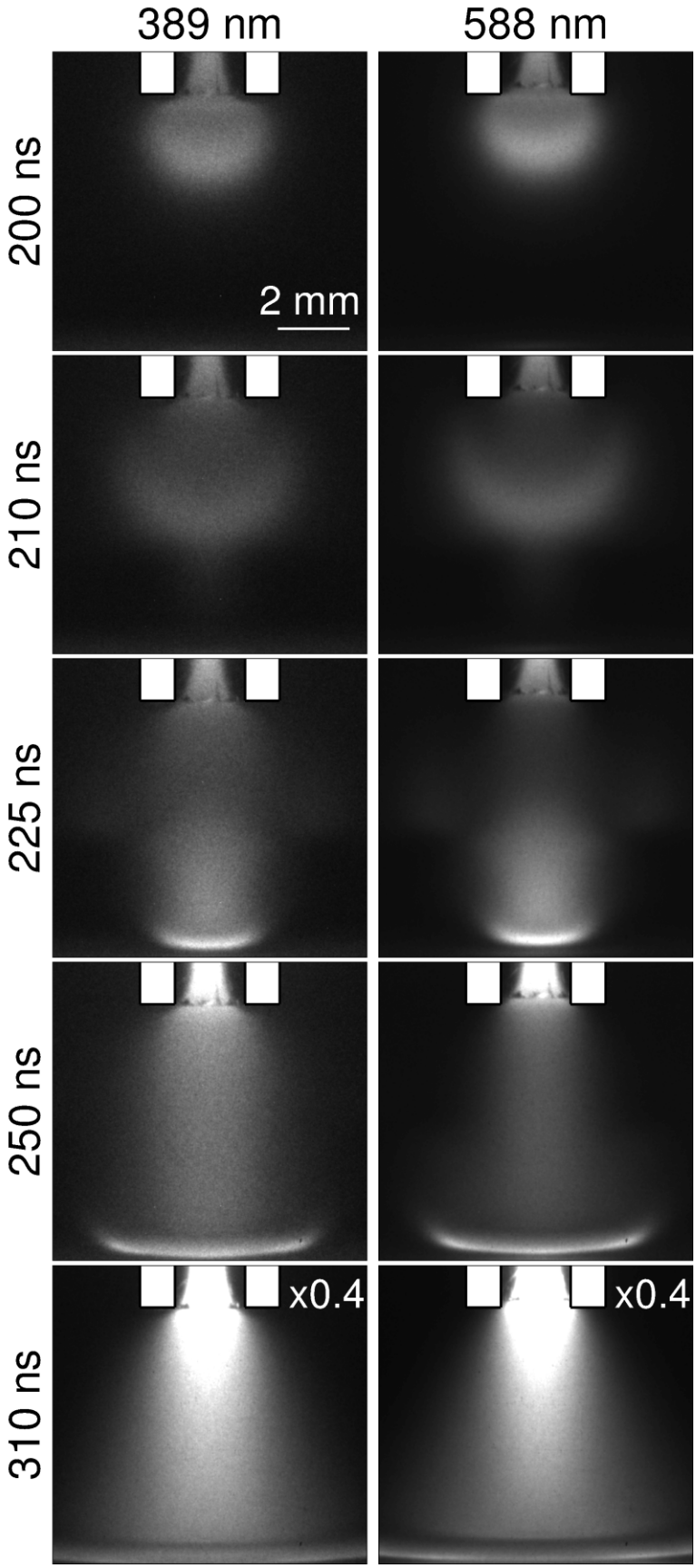

Lietz et al
Jet controlled
Fig 6 of 23

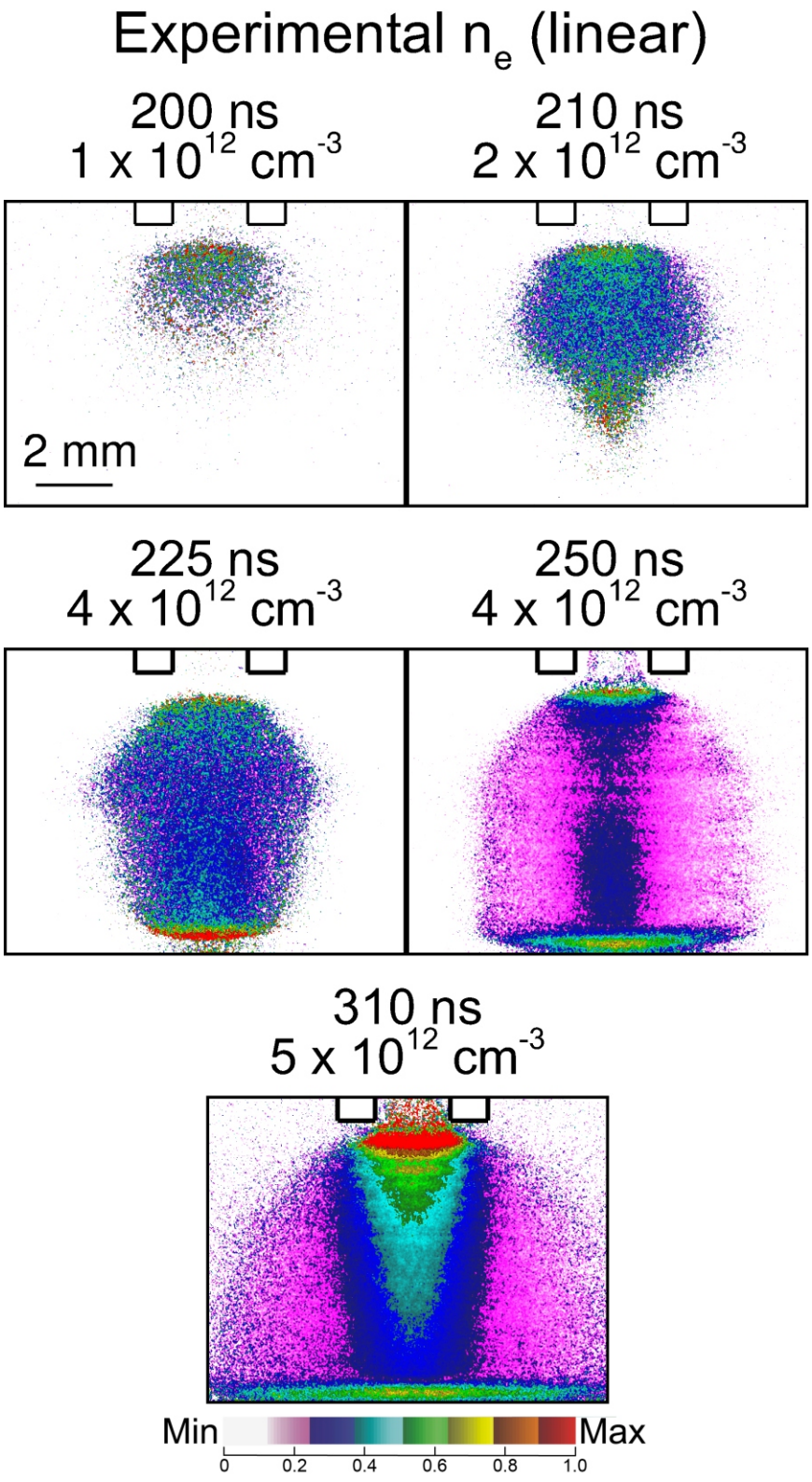

Lietz et al
Jet controlled
Fig 7 of 23

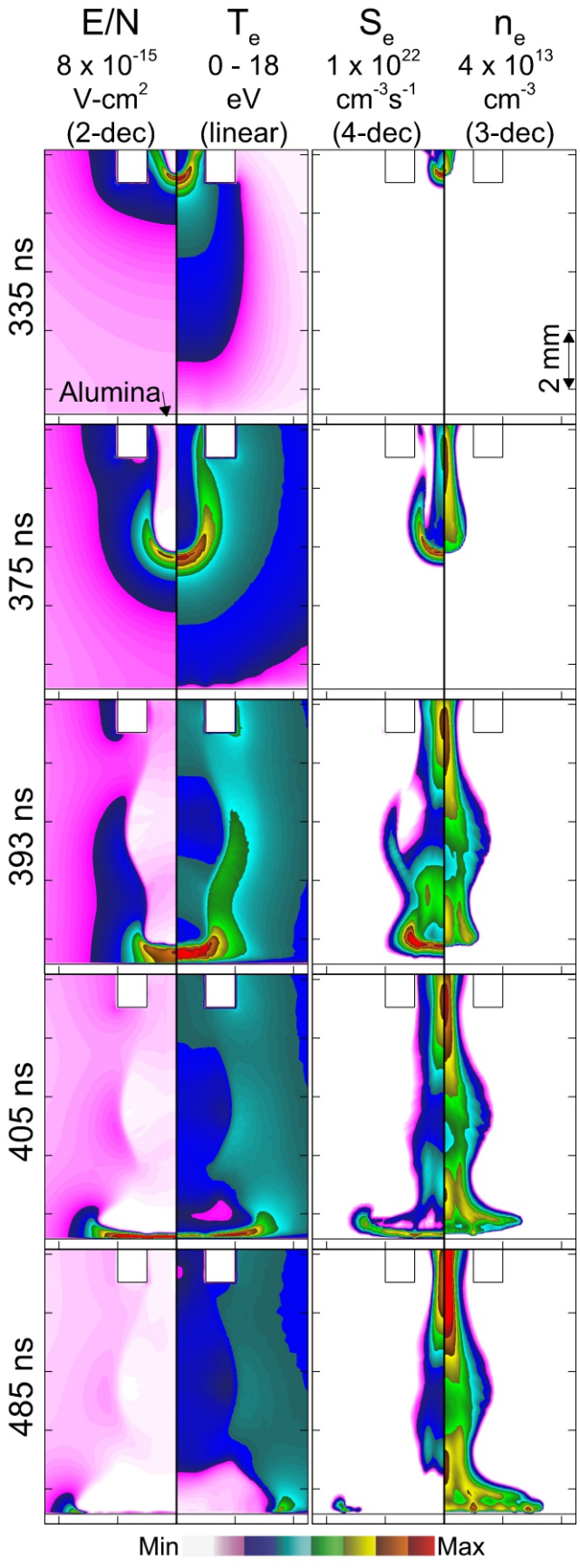

Lietz et al
Jet controlled
Fig 8 of 23

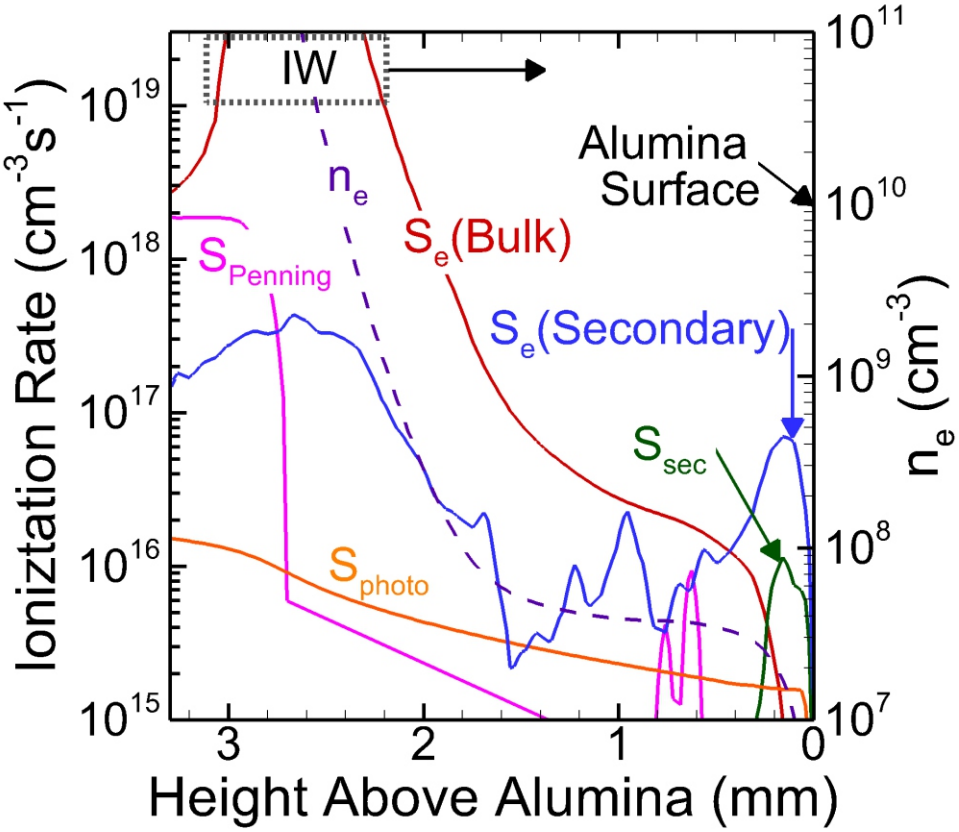

Lietz et al
Jet controlled
Fig 9 of 23

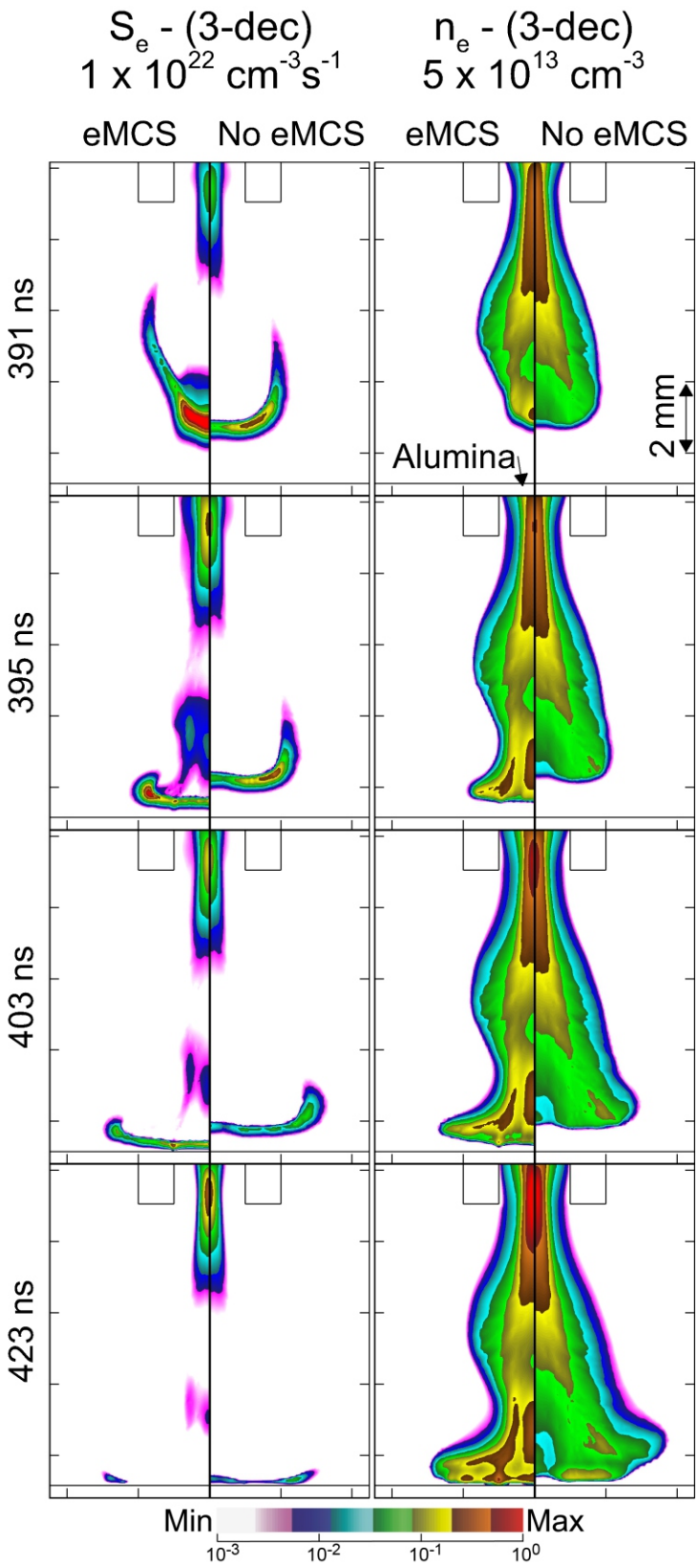

Lietz et al
Jet controlled
Fig 10 of 23

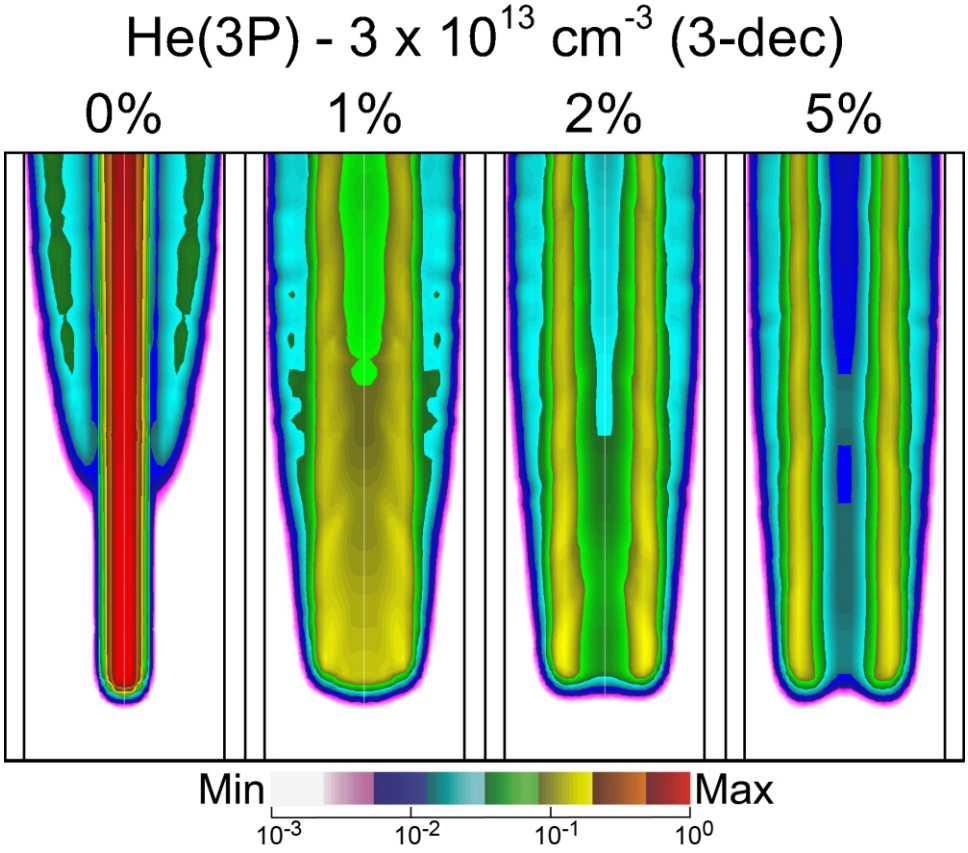

Lietz et al
Jet controlled
Fig 11 of 23

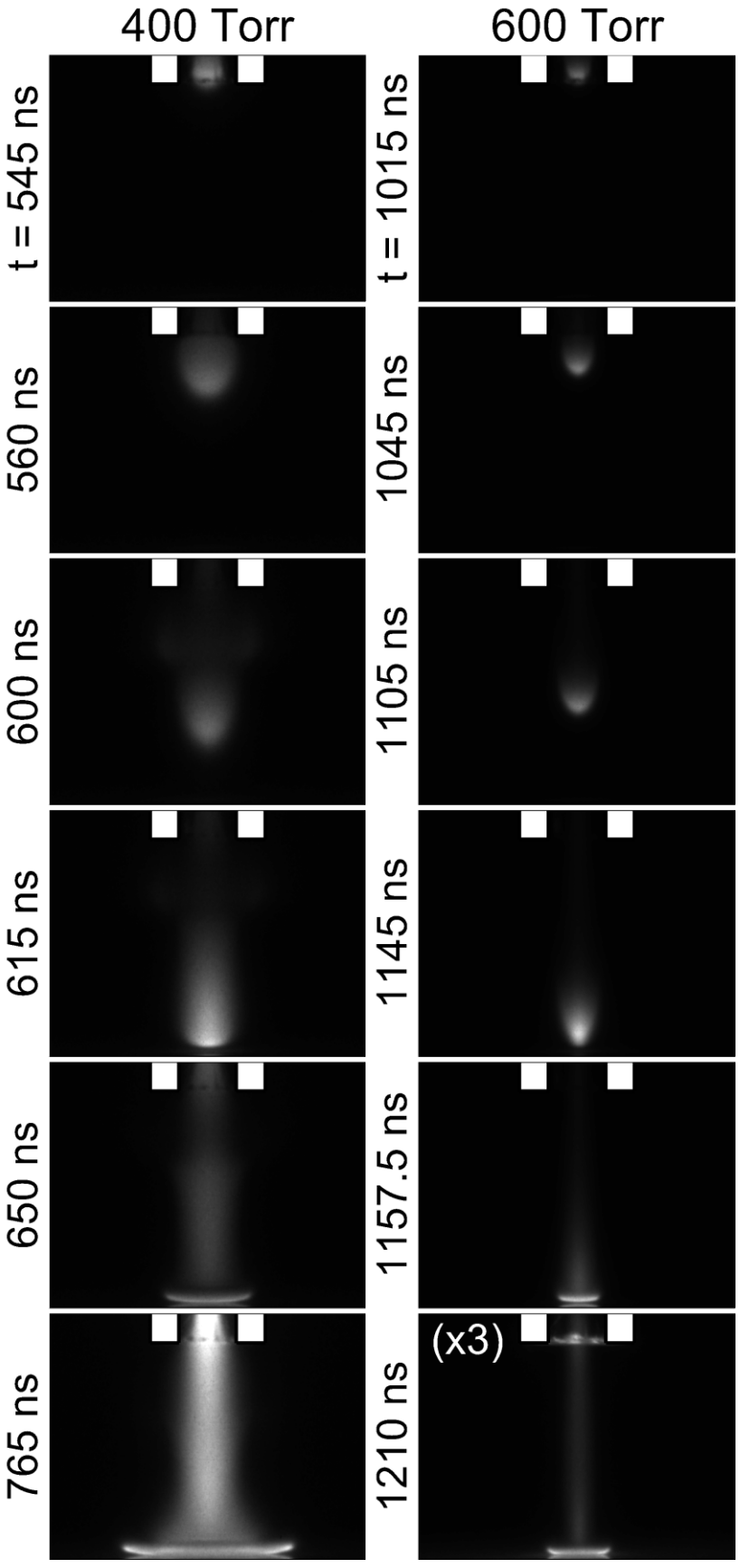

Lietz et al
Jet controlled
Fig 12 of 23

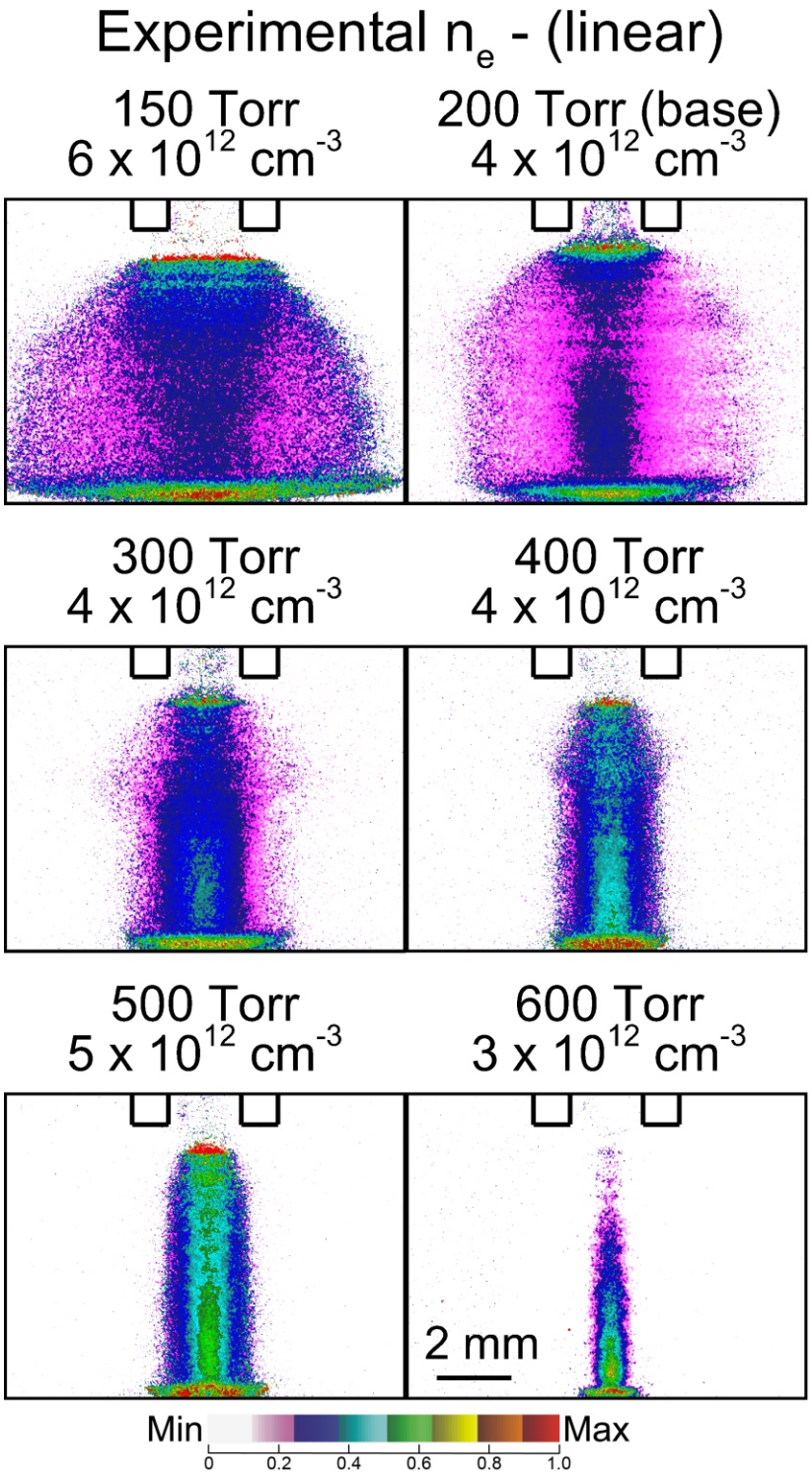

Lietz et al
Jet controlled
Fig 13 of 23

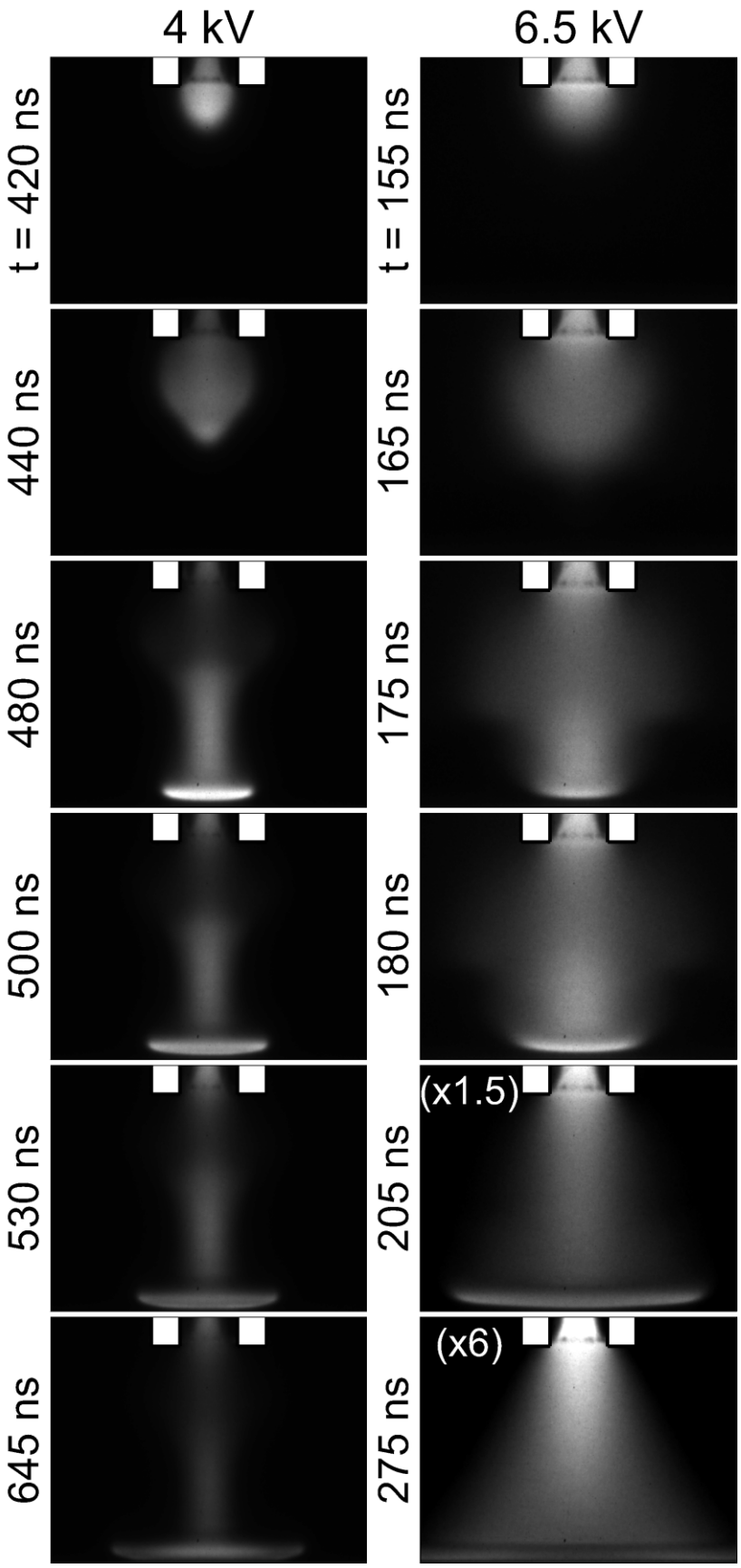

Lietz et al
Jet controlled
Fig 14 of 23

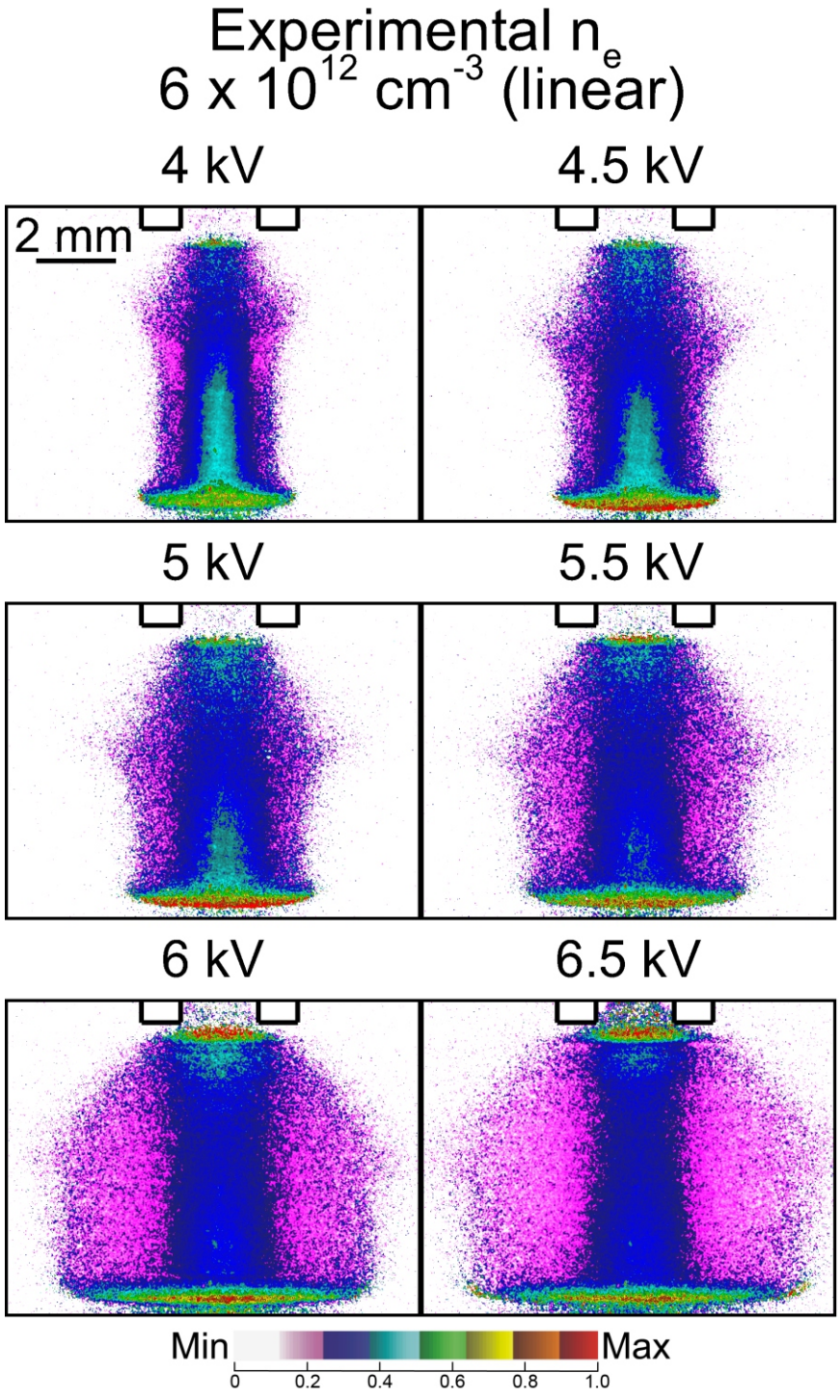

Lietz et al
Jet controlled
Fig 15 of 23

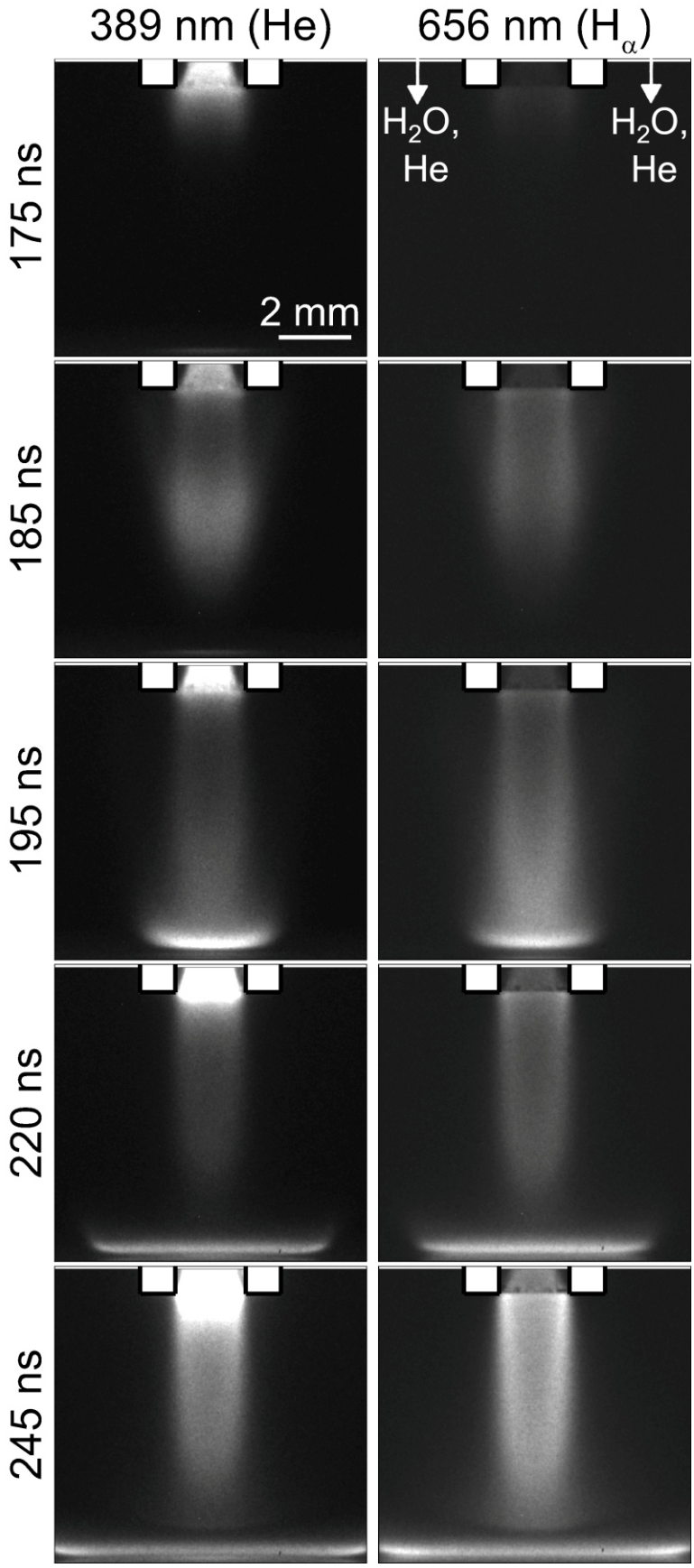

Lietz et al
Jet controlled
Fig 16 of 23

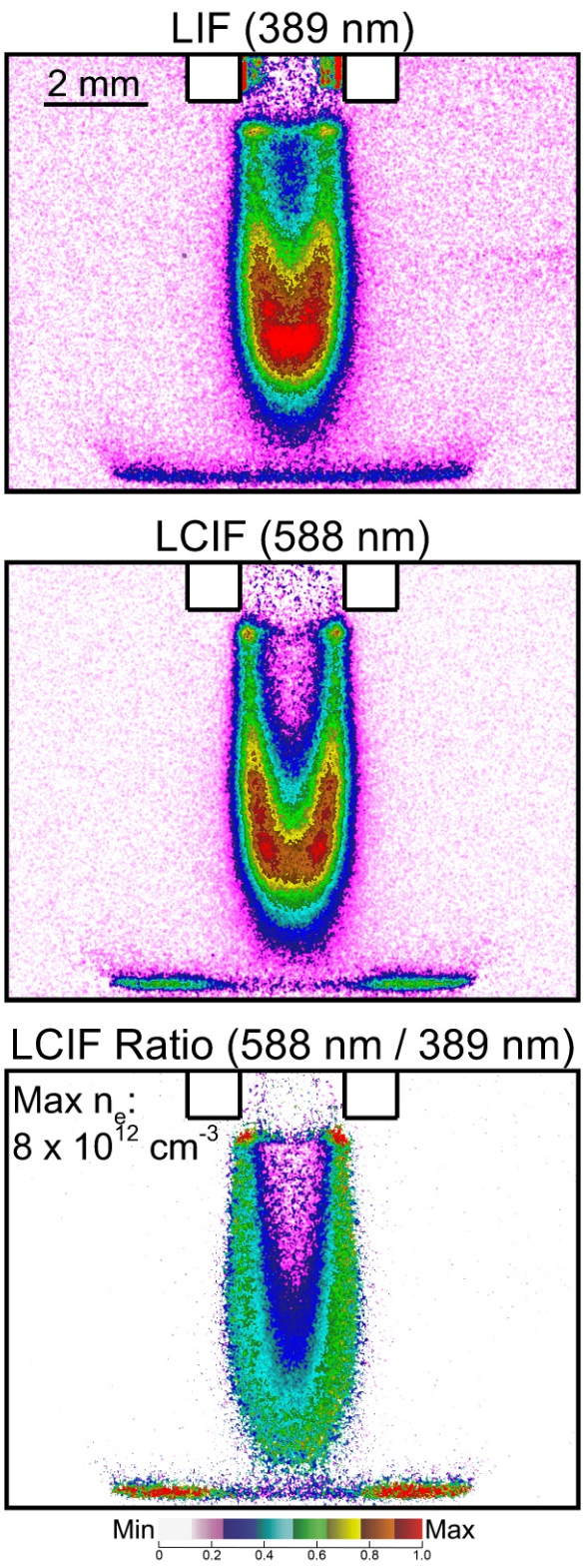

Lietz et al
Jet controlled
Fig 17 of 23

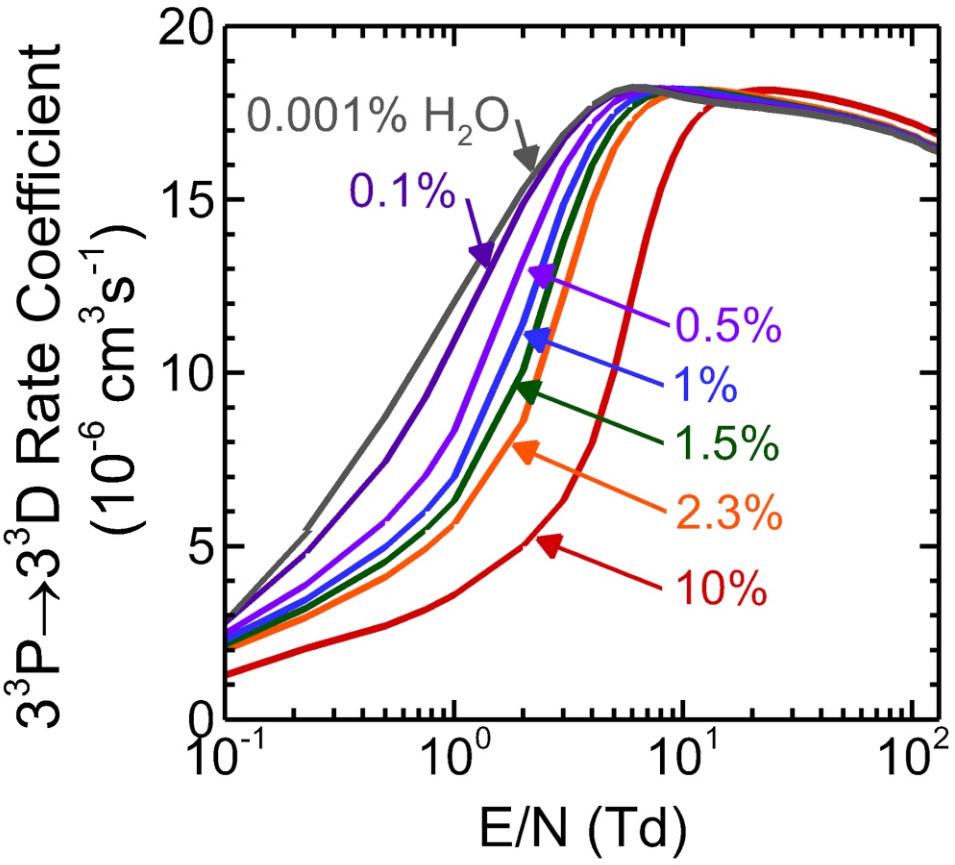

Lietz et al
Jet controlled
Fig 18 of 23

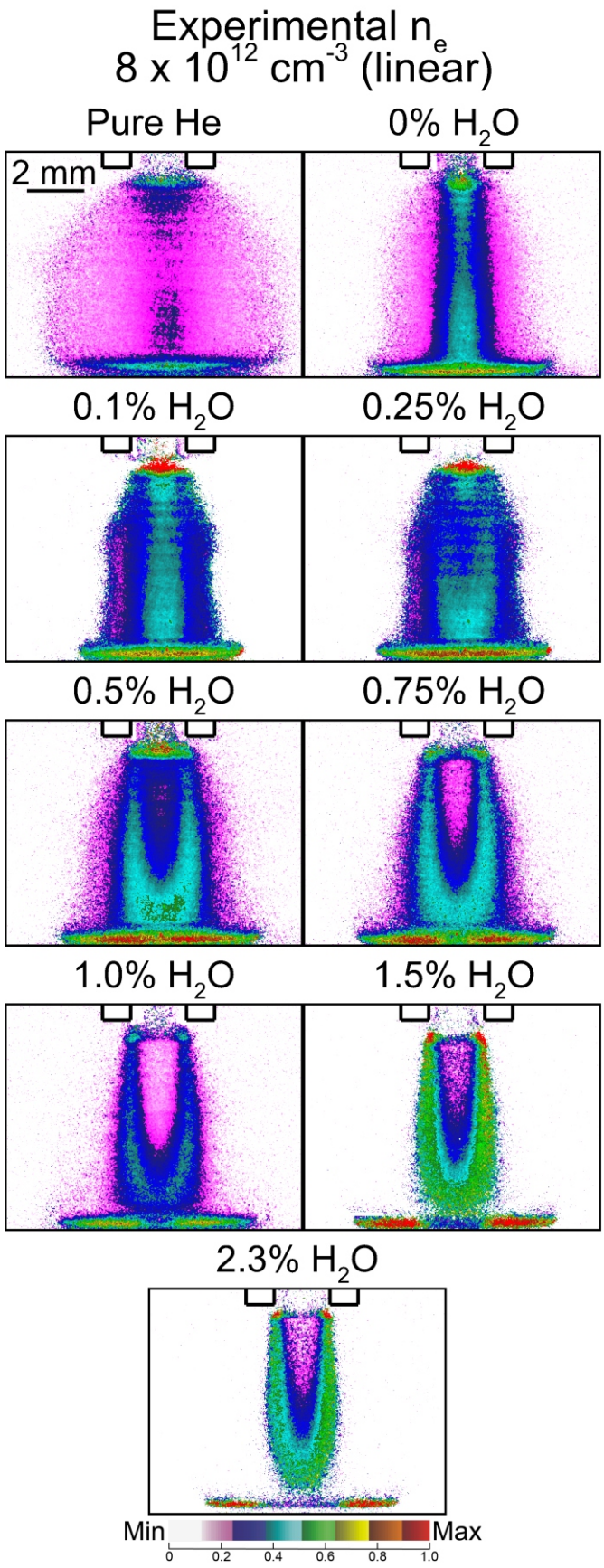

Lietz et al
Jet controlled
Fig 19 of 23

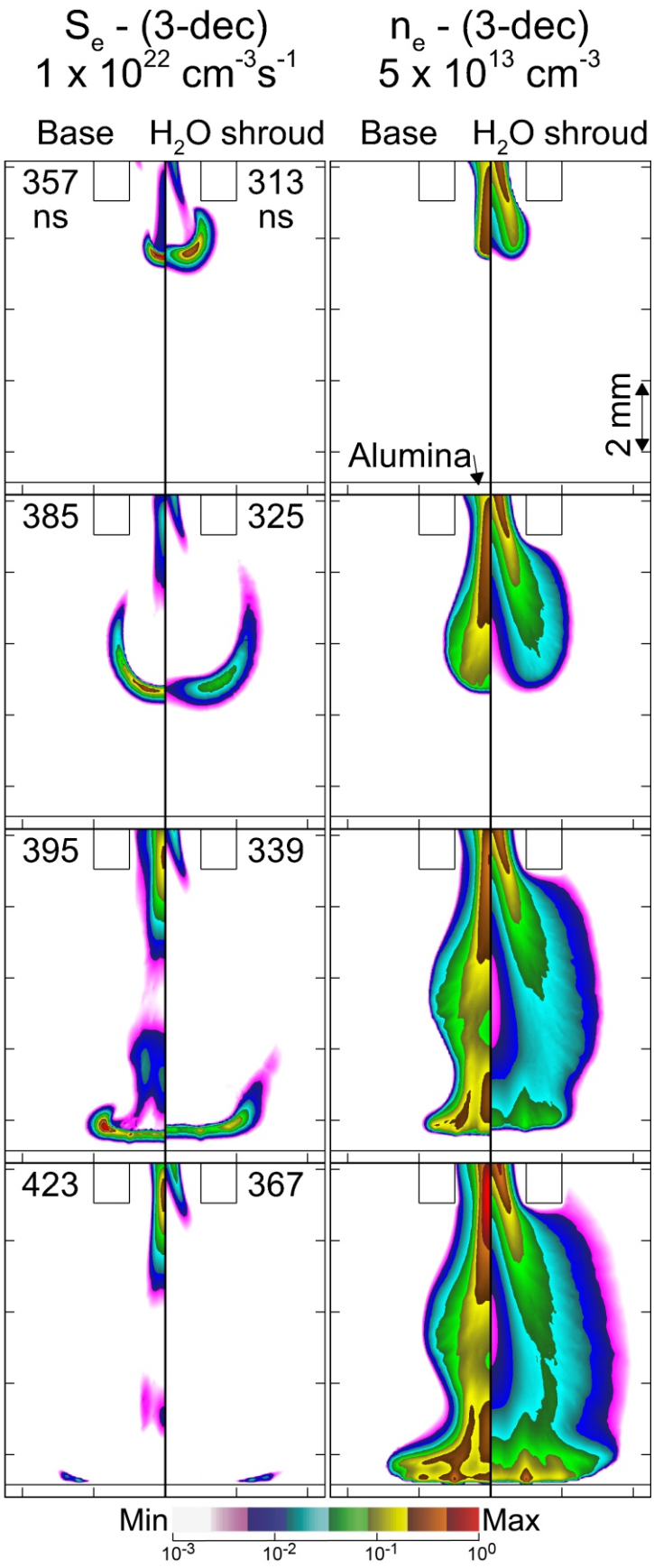

Lietz et al
Jet controlled
Fig 20 of 23

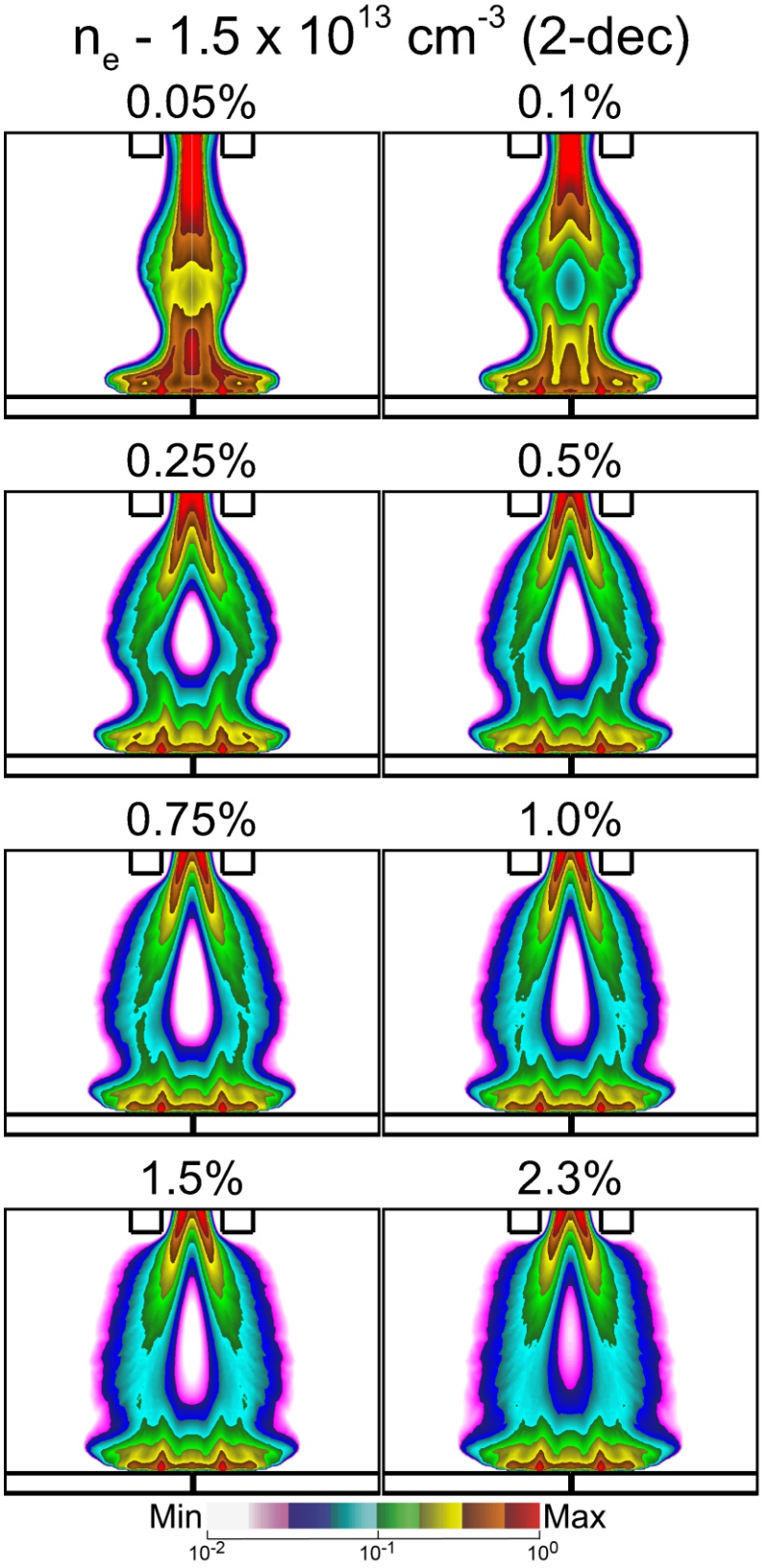

Lietz et al
Jet controlled
Fig 21 of 23

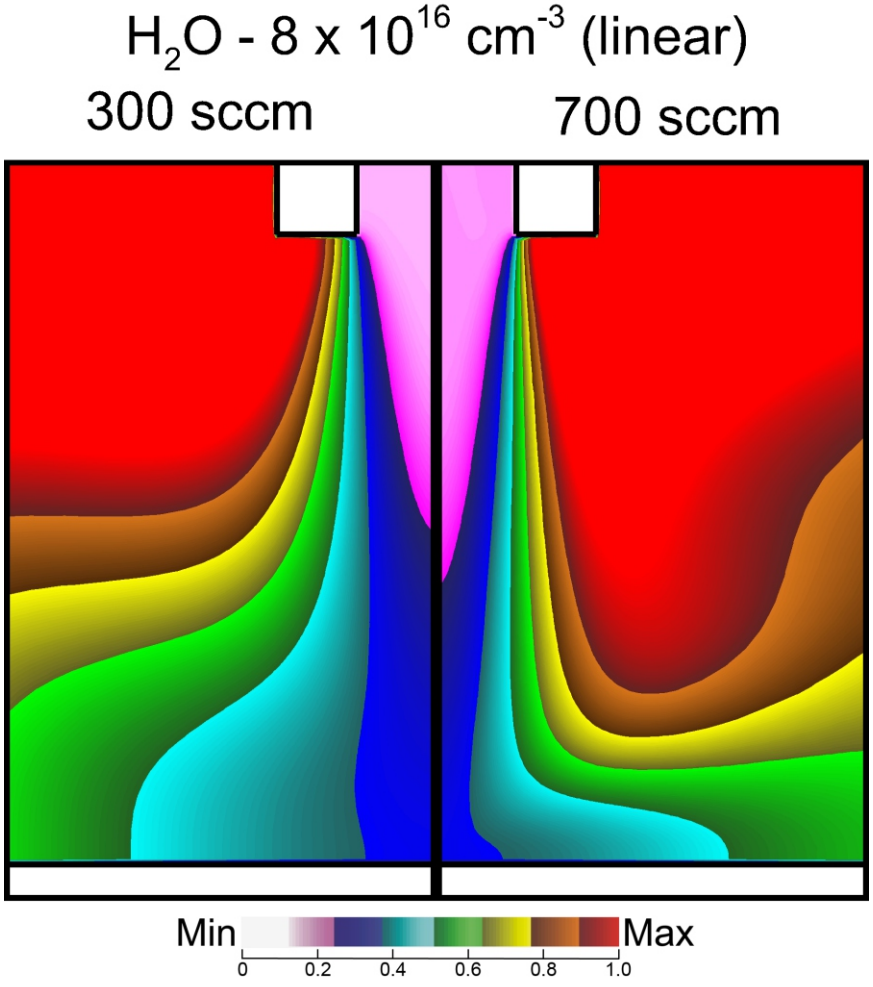

Lietz et al
Jet controlled
Fig 22 of 23

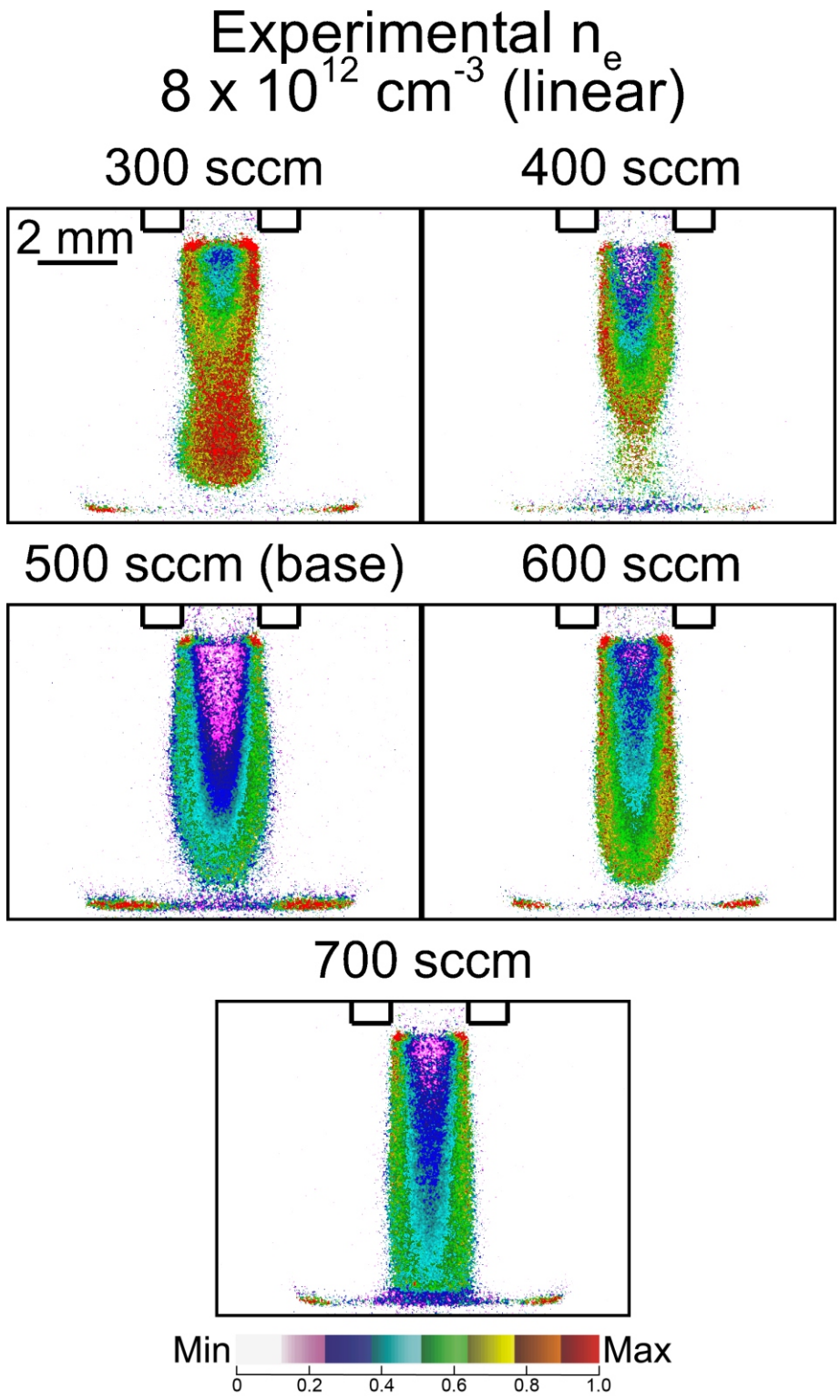

Lietz et al
Jet controlled
Fig 23 of 23